

University of Pécs

Doctoral School of Physics

Laser physics, nonlinear optics, and spectroscopy
Program

**The Effect of Intense Terahertz Pulses on *Eisenia
andrei* Earthworm Tail Regeneration**

Ph.D. Dissertation

Mahmoud Hasan Abufadda

Supervisors:

Prof. József András Fülöp

Assoc. prof. László Molnár



PÉCS, 2022



Contents

1. Introduction.....	1
2. Background	5
2.1. Interaction of electromagnetic radiation with biological tissue	5
2.2. Interaction of THz pulses with biomolecules	7
2.2.1. Water	7
2.2.2. Amino acids, peptides, and proteins	9
2.2.3. Deoxyribonucleic acid (DNA)	9
2.3. Effect of THz pulses on cells and tissues	10
2.3.1. Cells.....	10
2.3.2. Tissues	11
2.4. Effects of visible light and NIR on the regeneration capacity	12
3. Anatomical and biological properties of earthworm	15
3.1. Regenerative capacity in animals.....	17
3.2. Regenerative capacity of earthworm.....	18
4. THz pulse generation and measurements	21
4.1. THz generation.....	21
4.1.1. Optical rectification and tilted pulse front.....	21
4.1.2. Photoconductive antennas	24
4.2. THz pulses characteristics and measurements	24
4.2.1. Power/Energy measurements	24
4.2.2. Electro-optic sampling	25
4.2.3. Time-domain THz spectroscopy.....	27
5. Infrared and green optical pulses	28
5.1. Infrared pulses from an Yb laser.....	28
5.2. Second harmonic generation (green light)	29
6. Scientific goal.....	30
7. Results	32
7.1. Terahertz pulses induce segment renewal of the earthworm <i>Eisenia andrei</i>	32

7.1.1. Experimental animals.....	32
7.1.2. Ablation of tail segments.....	32
7.1.3. Further handling and experimental treatment of worms.....	33
7.1.4 Characteristics of the applied irradiation pulses.....	34
7.1.4.1. THz pulses.....	34
7.1.4.2. Green light.....	37
7.1.5. Regeneration blastema formation and kinetics of segment regeneration.....	37
7.1.6. Histological investigations.....	37
7.1.7. Calculation of the mitotic index (MI) characteristic for distinct body parts.....	38
7.1.8. Statistics.....	38
7.1.9. Experimental results.....	39
7.1.10. Discussion.....	44
7.1.11. Conclusion.....	50
7.2. Absorption of pulsed terahertz and optical radiation in earthworm tissue and its heating effect.....	51
7.2.1 Optical and THz transmission measurements.....	51
7.2.2 Tissue samples.....	52
7.2.3 Experimental results.....	53
7.2.4 Discussion.....	57
7.2.5. Conclusion.....	63
8. Thesis statements.....	65
9. Tézispontok.....	67
10. Publication list.....	69
11. Acknowledgment.....	70
12. References.....	71

Abbreviations

THz	: Terahertz
TDTS	: Time-domain THz spectroscopy
AChE	: Anti-acetylcholinesterase enzyme
BBO	: Beta Barium Borate crystal
IR	: Infrared
BSA	: Bovine serum albumin
BW	: Body wall
BV	: Blood vessel
cM	: Circular muscles
D ₂ O	: Deuterium oxide (Heavy water)
cDNA	: Complementary Deoxyribonucleic acid
EOS	: Electro-optic sampling
ECM	: Extracellular matrix
EMR	: Electro magnetic radiation
EPDCs	: Epicardial-derived cells
FWHM	: Full width at half maximum
hESCs	: Human embryonic stem cells
HUVEC	: Human umbilical vein endothelial cells
H2AX	: Histone protein breaks in DNA
LN	: Lithium niobate
LLLT	: Low-level light therapy
MGE	: Midgut epithelium
MOPA	: Master oscillator power amplifier
MI	: Mitotic index
OR	: Optical rectification
VNC	: Ventral nerve cord

1. Introduction

The electromagnetic spectrum (EMS) encompasses a wide variety of wavelengths and frequencies. It is separated into several regions. Radio waves, microwaves, terahertz (THz) waves, infrared (IR), visible light, ultraviolet (UV), X-rays, and gamma rays are examples of wavelengths that decrease or increase photon energy and frequency. THz waves have frequency ranging from 0.1 to 10 THz and wavelengths ranging from 3 mm to 30 μm . THz radiation is a band of electromagnetic radiation [1], which is located between microwaves and IR radiation (Figure 1-1), and shares some characteristics with each of them. THz waves are nonionizing, noninvasive, and able to penetrate a wide range of materials with a penetration depth of that is typically shorter than that of microwave radiation [2].

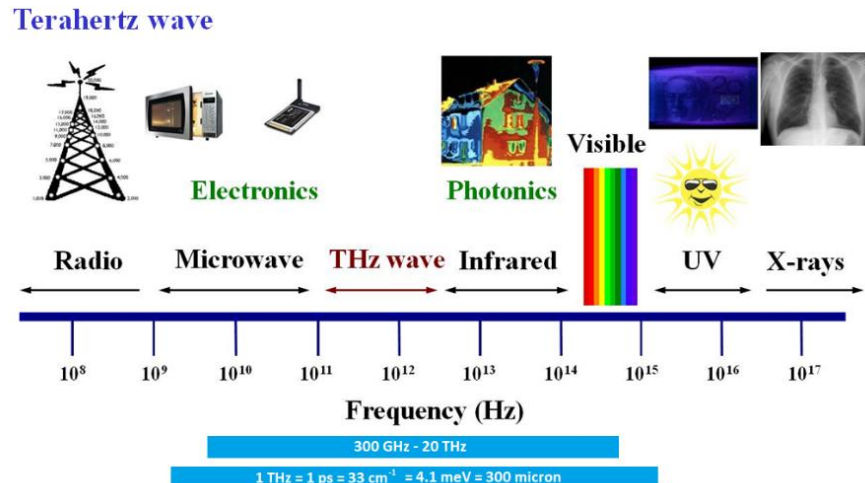


Figure 1-1. THz band in the electromagnetic spectrum [3].

Electromagnetic radiation's influence on living organisms is a complex process. Electromagnetic fields, according to a previous study, have a wide variety of complex impacts on vital molecules (DNA, ionic channels, and some proteins), as well as the nervous system and other organs' activities [4]. Several theories have been proposed

to explain the effect of electromagnetic frequency on living organisms via induction, resonance, and radical mechanisms, influencing cell signal transmission, biological membrane structure and ion transport, nucleic acid replication and transcription, protein synthesis, and cell proliferation processes [5], [6].

Chronic weariness, cataracts, chest pain, cardiovascular and reproductive system abnormalities, central nervous system endocrine disorders, and immune system disorders are all possible side effects of EMR *in vivo*. It also has been linked to leukemia, brain cancer, lung and breast tumors, genotoxicity and neurodegenerative illness, infertility, birth defects, depression, suicide, and Alzheimer's disease in humans. [7].

The application of THz radiation in medicine and biology has recently grown rapidly as a novel interdisciplinary field. Several studies investigated the biological effects of THz radiation on biomolecules, like DNA, RNA, and proteins, as well as on human tissues and cells, often resulting in contradictory experimental results [8]. THz waves, on the other hand, can influence the activity of biomolecules or cells through thermal or non-thermal biological effects, according to consensus. The former was found to be hazardous, resulting in cell death (apoptosis, necrosis) [9],[10], or morphological injury of neurons in *in vitro* experiments [11], and expression of stress molecules (heat shock proteins, DNA damage markers) in irradiated cells [12].

Several non-thermal biological effects of 0.25–3.0 THz radiation were experimentally shown [13]. It can influence the plasma membrane permeability, resulting in either suppression or facilitation of neuronal activity [14]. Furthermore, it can accelerate cell differentiation and cellular reprogramming [15]. Based on these observations, THz radiation appears to have a powerful and complex effect on biological systems, which is highly dependent on the irradiation parameters (mean frequency, power, duration, electric field strength), and the morphological and/or physiological characteristics of the biological targets [16].

In contrast to the *in vitro* experiments, the effects of THz exposure on living organisms have received relatively little attention. The *in vivo* biological effects of

pulsed THz radiation on the skin wound of mice revealed that repeated THz exposure disrupted the wound healing process, which is dependent on cell proliferation and differentiation. Kim et al. found that wound responses were predominantly mediated by transforming growth factor-beta (TGF- β) signaling pathways [17]. Since THz radiation is used more frequently in biology and medicine, it is important to learn about and understand its effects (both positive and negative) at the organism level in *in vivo* experiments.

The regeneration of surgically ablated tail segments of earthworms is a reasonably easy *in vivo* experimental procedure that has been employed since the 18th century. Earthworms have a remarkable ability to regenerate missing tail segments [18], and this process is mediated by some internal and external factors. Morgan [19] advocated for the regeneration's neuronal reliance, suggesting that certain neural factors like neurotransmitters and neurohormones were necessary for the formation of a regeneration blastema from which the new segments were formed. The influence of the immune system on the formation of the regeneration blastema and renewing structures was shown as well [19], [20]. The effects of the internal factors on cell proliferation, differentiation, and tissue morphogenesis can be modified by certain environmental conditions, such as temperature [21], osmotic stress [22], and electromagnetic waves like laser irradiation [23].

Studying the effects of intense THz pulses of μJ -level energy on the renewal properties of earthworms is a promising approach to explore the influence of pulsed THz radiation on biological cells and tissues *in vivo*. The regenerative potential of animals and specific THz interactions on biological systems, on the other hand, are still unclear.

However, some experimental evidence suggests that anatomical, physiological, and cellular variables influence segment regeneration kinetics. [24]. In this research, the effect of THz irradiation on the regeneration segment kinetics of ablated *Eisenia andrei* earthworms was investigated. The formation of new segments, consisting of different tissues, depends on the mitotic activity of the cells, followed by the growth and

differentiation of the daughter cells to specific tissue cells, hence, the migration of certain blast cells to the injury site has also been observed [22,23]. The rebuilding of the experimental animals' original body plan is determined by the strength of segment development. Proliferation and growth/differentiation of cells are genetically dictated processes that have only been partially studied and understood [24]. The regeneration of the segment, on the other hand, can be quantified as a result of molecular, cellular, and histological changes. As a result, the earthworm regeneration model is an excellent tool for investigating the effects of THz radiation on cells and tissues at the organism level. Another objective was to see how THz and optical pulses interacted with biological tissues.

The following is a breakdown of the dissertation's structure. Chapter 2 describes the basics of electromagnetic radiation interaction with living organisms, and the biological effects of THz radiation. Chapter 3 introduces the animal model *Eisenia Andrei* earthworm. Chapter 4 gives an overview on the generation and detection of THz pulses. It discusses various pulsed THz sources (optical rectification, the tilted-pulse-front technique, photoconductive antenna), and THz pulse measurement techniques (pyroelectric power measurement, pyroelectric camera, time-domain THz spectroscopy, electro-optic sampling, photoconductive antenna as detector). Chapter 5 discusses the IR and green light optical characteristics, and their effects on biological cells and tissues. The scientific goals are established in chapter 6. Chapter 7 discusses the research findings, which are separated into two categories. First, it is shown that THz pulses can induce segment renewal via cell proliferation and differentiation, overriding the endogenous regeneration program of the earthworm *Eisenia andrei*. Second, absorption of pulsed THz and optical radiation in biological tissues and its heating effect are investigated. Chapter 8 contains the thesis statements, chapter 9 is t ezisontok, chapter 10 is the publication list of the author. Chapter 11 is acknowledgment, and chapter 12 is the references list.



2. Background

2.1. Interaction of electromagnetic radiation with biological tissue

The interaction of electromagnetic radiation, ranging from X-ray to radio-waves, with living systems can be investigated at various levels of organization of a living organism: molecular, cellular, organ, system, or an entire body. One of the most important steps in analyzing the effects of specific radiation exposure in a living organism is the assessment of the induced internal electromagnetic field and its spatial distribution. THz and IR interactions with in vivo earthworm animals and in vitro earthworm tissues were the focus of this research.

The most commonly researched mechanism in the interaction of electromagnetic fields with biological systems is the absorption of electromagnetic radiation power. The transition of radiation energy into another kind of energy, such as heat, sound, fluorescence, and so on, occurs when electromagnetic radiation is absorbed. Absorption centers, which are particles or molecules that absorb radiation, make up an absorbent medium. [25]. The absorption of a (homogenous) medium can be characterized by the absorption coefficient μ , defined as the reciprocal of the thickness x over which radiation of intensity I_0 is attenuated to:

$$I(x) = \frac{I_0}{e} \approx 0.37 I_0. \quad (1)$$

The variation of the intensity as function of the light propagation distance x in a homogenous medium follows the well-known Beer–Lambert law [26]–[28]:

$$I(x) = I_0 \exp(-\mu x), \quad (2)$$

where $I(x)$ is the intensity of transmitted light, given, for example, in the unit W/cm^2 . The unit of μ is typically expressed in cm^{-1} . Biological tissues are

heterogeneous media with different levels of organization that include cells, cell organelles, and impurities [29]. However, in many practical cases their absorption properties can be well characterized by an effective absorption coefficient.

Absorption is just one of various ways electromagnetic radiation interacts with tissue to induce photothermal and photochemical reactions, which then lead to a cascade of biological effects. Scattering, reflection or transmission can cause neither photothermal nor photochemical reactions. The construction of an acceptable optical model accounting for light scattering and absorption is crucial given the enormous diversity and structural complexity of tissues (Fig. 2-1) [30]. Scattering in a medium can be characterized by the scattering coefficient μ_s . In a nonabsorbent sample, it is defined as the reciprocal of the thickness x over which light of intensity I_0 is attenuated (due to scattering) to 37% (Eq. (1)). The intensity variation follows an exponential law similar to Eq. (2), with μ replaced by μ_s .

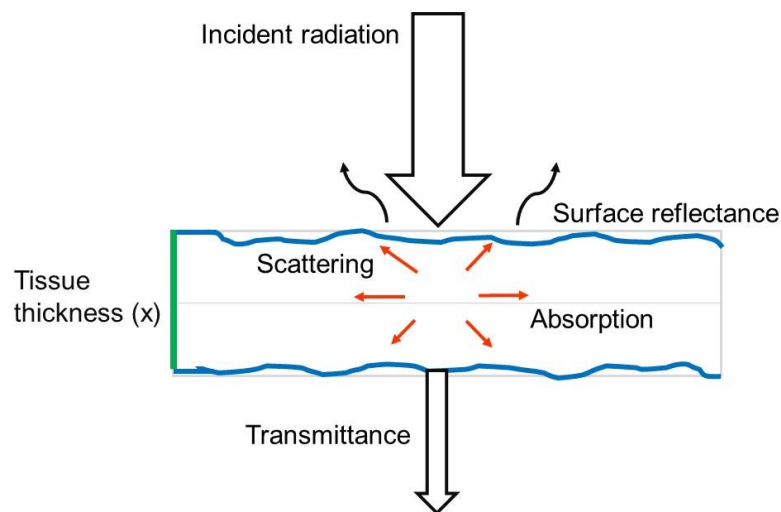


Fig. 2-1. Schematic representation of different mechanisms of radiation interaction with tissue.

Biological tissue is a dielectric medium with a greater average refractive index than that of air. The refractive index is defined by $n = v/c$, where v and c are the (average) speed of light in the tissue and in air, respectively. At the tissue-air interface, partial reflection (Fresnel reflection) occurs (Fig. 2-1) [26], [31]–[33]. The

direction of light propagation is changed by refraction when it passes obliquely from one medium into another with different (refractive indices) [25]. Finally, it is concluded that the electrical behavior of the tissue (dielectric properties and conductivity) is highly dependent on the water content and the relative amounts of free and bound water present [34]. Understanding the factors that influence body temperature as a result of electromagnetic radiation absorption justifies a study of the various heat pathways within the body [35].

2.2. Interaction of THz pulses with biomolecules

To understand the interaction between THz radiation and biological molecules, cells, and tissues, it is important to use an appropriate theoretical framework. In line with most interactions with tissue, it is the electric field that is of key significance. One approach is to use a classical EM wave description which characterizes the medium in terms of the permittivity ϵ (the ability of the medium to be polarized) and conductivity σ (the ability of ions or electrons to travel through a medium). These parameters describe, in macroscopic terms, the interaction with ensembles of molecules, including water and proteins. The photon energy of THz radiation is in the range of 2.0×10^{-22} to 1.3×10^{-22} J, and therefore in the range of energies associated with transitions between molecular energy levels [36].

2.2.1. Water

Because water is a polar molecule, it absorbs a lot of THz radiation, and many researchers have tried to characterize its absorption spectrum in the THz regime. Water's polarity also indicates that it is active in the infrared spectrum. The various vibration and liberation modes of water are shown in Fig. 2-2(a). The frequencies of the ν_1 , ν_3 , and ν_2 vibrations lie in the mid- to far-infrared. In liquid water, the infrared and Raman spectra are complicated by vibrational overtones and combinations with liberations. The liberations are best described as restricted rotations with a rocking motion. Hydrogen bonding also complicates the situation. Hydrogen bonds are

weaker than covalent (intra-molecular) bonds, and their bond lengths are significantly larger (1.97 Å versus 0.96 Å, see Fig. 2-2(b)), resulting in modes at THz frequencies in [37].

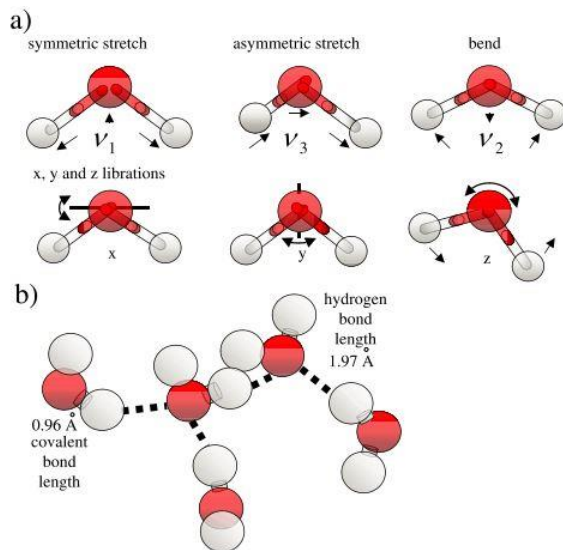


Figure 2-2. (a) The vibration and libration modes in water. (b) A schematic diagram to illustrate the differences between intra- and inter-molecular bonding in water [37].

The vibrational and librational absorption spectra of liquid water has been assigned to a variety of modes [38]. Bursulaya and Kim investigated the mode at 1.8 THz (60 cm^{-1}) by comparing the spectrum of heavy water (D_2O) with that of normal water [39]. The mode was insensitive to isotope substitution, implying that it is primarily caused by oxygen motions. This, along with findings indicating rotation, showed that the model had to be a mix of rotation and translation motions. As a result, an H-bond bend was assigned to the model. According to instantaneous normal mode theory, the 1.8 THz (60 cm^{-1}) band is caused by a bending type motion transverse to the hydrogen bonds [40]. Rather, it is caused by the rattling motion of a single molecule within a cage of surrounding molecules. This cage analogy serves as the foundation for comprehending the assignment of relaxation processes to liquid water. Water must be described using at least two relaxation processes [41], and these can be modeled as oscillators using Debye theory [42], which couples polarization

relaxation to the electric field and serves as the foundation for polar liquid simulations for understanding THz interactions with tissue [43].

2.2.2. Amino acids, peptides, and proteins

Since the structure represents a large dipole, neutral solutions of amino acids should exhibit a high permittivity (as permittivity reflects the degree of polarization). Because there are no molecular interactions between the solute and the solvent, the measured relaxation of glycine (the simplest α -amino acid) is slower than that calculated. The observed characteristic frequency for glycine is 3.3 GHz rather than 12.56 GHz. For a single relaxation process, in the THz region, the complex permittivity is given by ϵ^∞ [44]. Since amino acid molecules are unable to respond to the rapidly changing THz electric field via bulk rotation, the interaction between THz radiation and amino acid solutions is dominated by the interaction between molecular rotational and vibrational modes.

Proteins comprise one or more polypeptide chains folded in a complex geometry [45]. Lee demonstrated that via absorbing THz waves, the bacteriorhodopsin membrane protein molecule changed its conformation, and the conformational change can be detected by observing the vibrational modes in the THz region [46].

2.2.3. Deoxyribonucleic acid (DNA)

In this research, the influence of THz pulses on DNA molecules, and THz genotype effects as mentioned in the introduction was not investigated, however, a summary of recently investigated mechanisms is discussed. A simple lattice dynamical model was successful in explaining the low-lying vibrational modes and in a semi-quantitative description of the influence of hydration on mode frequencies. Low-frequency vibrational modes occurring in DNA are associated with the collective motion of tertiary subunits moving concerning one another, or coherent movement of a portion of a structural subunit [47]. Another study confirmed that a large number of low-frequency collective modes exist in the frequency range 0.1–2 THz. The time-resolved

THz transmission analysis of polynucleotides confirms that the complex refractive index is strongly dependent on the hybridization state of DNA molecules (double- or single-stranded DNA) [48].

Furthermore, it was shown that merely ten minutes of THz pulse irradiation can generate a considerable increase in H2AX phosphorylation, implying that THz pulse irradiation may cause DNA damage in exposed skin tissue [49]. Specific THz radiation exposure may have a significant impact on the natural dynamics of DNA, influencing complex molecular processes such as gene expression and DNA replication [50]. In contrast, some other studies found that THz radiation at 0.38 THz and 2.52 THz did not lead to DNA damage in skin cells in vitro [51]. THz irradiation did not induce the formation of γ H2AX foci or structural chromosomal aberrations in human embryonic stem cells (hESCs) [52].

2.3. Effect of THz pulses on cells and tissues

2.3.1. Cells

The in vitro and in vivo experiments were generally conducted at frequencies below 0.15 THz, with low power and short exposure time (10–30 min). THz radiation impacts on mammalian cells were not demonstrated in these experiments. In addition, human lymphocytes were found to have potential genotoxic and epigenetic effects, as well as changes in liposome membrane permeability. The specific irradiation settings required to elicit these effects, on the other hand, remain unknown. According to recent research, following a 6-hour exposure period, a modest THz field can trigger genetic instability in human lymphocytes [53]. No effect was observed on the mitotic index or morphology of the hESCs following THz exposure [52]. Furthermore, there was no difference in THz radiation on different types of human epithelial cells and embryonic stem cells morphology, attachment, proliferation, and differentiation between irradiated and control cell cultures. On other hand, during certain experimental conditions, the cells were capable of compensating for any effects caused by exposure

to THz radiation with the peak power levels [54]. Additionally, it was reported that neurons briefly exposed *in vitro* to powerful THz radiation (over 30 mW/cm²), at a specific frequency, may develop changes in the morphology of the cellular membranes and intracellular structures [11].

Bock et al. reported that THz radiation promoted cell development toward the adipocyte phenotype, and it had been seen the cell cultures grew over time after being exposed [15]. *In vivo* THz radiation can cause a similar neurotransmitter release from neurons, promoting the formation of the regeneration blastema and cell differentiation. Despite this, Borovkova et al. demonstrated that THz radiation has a dose-dependent cytotoxic effect on glial cells [55].

2.3.2. Tissues

The majority of research on the interaction of THz radiation with biological tissue has been done in the context of imaging, with the literature focusing on the ability of imaging to distinguish between different types or states of tissue. Images are based on fairly simple parameters, rather more than the detailed analyses sometimes used in spectroscopy. This is ideal for picture generation speed as well as the fact that macroscopic samples may not be heterogeneous. Images can be derived from either continuous wave or pulsed THz [53], THz pulsed imaging (TPI), which may be performed using either a reflection or transmission geometry, can give a set of images each with different contrast properties.

Tissue research is focused in two areas. The first is on diagnostic applications near the body's surface, which are likely to be the first performed due to the strong water absorption that limits the depth of penetration. Second, researchers have considered tissue that currently must be examined *in vitro*, by which, with technological advances, should be accessible in the future to THz irradiation [56].

In several studies, tissue absorption was found to be lower than that of pure water. This suggests that more image depth may be achievable than previously imagined. However, because sustaining hydration in samples that are equivalent to

the actual body is difficult, precise assessments may have to wait until the first in vivo research [57], [58].

2.4. Effects of visible light and NIR on the regeneration capacity

The influence of several wavelengths of a low-intensity light-emitting diode (LED) on the regeneration, stem cell proliferation, and expression of planarians freshwater flatworms has been studied. It was discovered that exposing regenerating planarians to low-intensity red light diodes for a single period increased head blastema growth in a dose-dependent manner (up to 40%). Planarians exposed to green light had the reverse effect, with the rate of head blastema development lowered by up to 21%. But planarians exposed to blue light had no effects on the process of head blastema growth [59].

Light radiation can affect wound healing and the regeneration of damaged tissues. Light exposure has been shown to modulate most phases of the wound healing process [60]. It has been reported that red (670 nm) and green LED light (530 nm) stimulates fibroblast growth and wound healing [61], [62]. Due to the activation of fibroblast migration and proliferation, as well as the proliferation of epithelial cells, light radiation (633 or 830 nm) can stimulate the proliferative phase in ischemic and diabetic wounds [63]. In addition, light exposure can modulate non-wound regenerative processes [60], [64]. Photobiomodulation's effects on bone regeneration processes have recently been reported. They have been shown to arise due to the effect of light on osteoblast proliferation, osteoclast activity, and bone tissue remodeling [65].

Low-level light therapy (LLLT) is becoming more popular in the fields of tissue regeneration and wound healing. Several in vivo studies have shown that LLLT has a beneficial effect on angiogenesis. Rohringer et al. studied the underlying features in vitro by comparing the effects of light therapy on endothelial cells using light-emitting diodes of various wavelengths. Thus, it is not surprising that there are discrepancies

between in vitro and in vivo studies [66]. On the other hand, in vitro investigations are valuable and necessary for determining the role and effects of specific cell types [67].

Fig. 2-3(A) illustrates the effects of LLLT in different wavelengths on both proliferation and cell metabolic activity of endothelial cells in human umbilical vein endothelial cells (HUVEC) after initial light treatment at 24 h, 48 h, and 72 h [66]. Cell proliferation was similar in all stimulated and non-stimulated groups within the first 48 hours after stimulation. There were no significant differences between any light-treated group and untreated controls after 24 and 48 hours. After 72 hours, however, stimulation with green and red light significantly increased HUVEC proliferation [66]. Blue light treatment showed only a 45% increase compared to the control group.

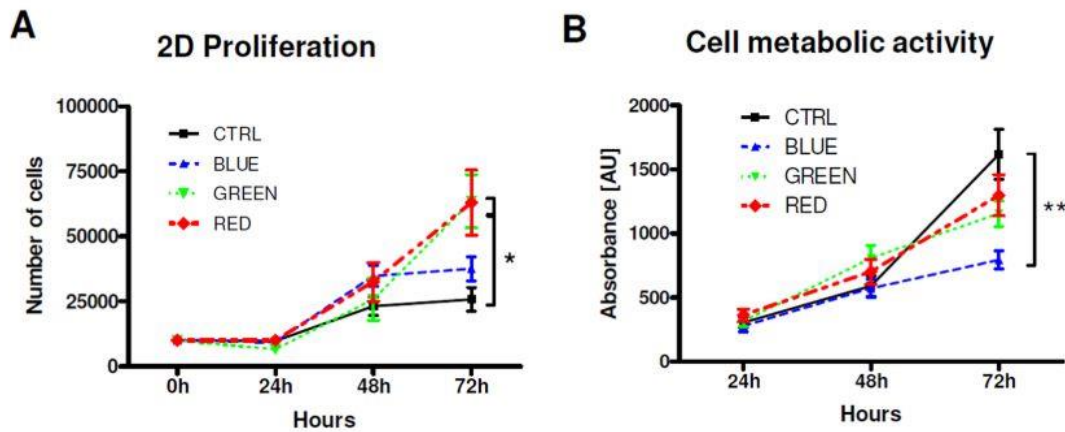


Figure 2-3. Effects of pulsed LED light on proliferation (A) and cell metabolic activity (B) of HUVEC cultured in a 2D cell culture model. Stimulation of HUVEC on day 0 with green and red light had no significant effect on metabolic activity while cell proliferation was significantly increased. In contrast, blue light significantly decreased metabolic activity and showed no effect on proliferation. * $P < 0.05$, ** $P < 0.01$ [66].

The effect of LED on the examined earthworm, like other higher animals and human species. In humans, the cholinergic system is involved in the basic functions of the skin like proliferation and differentiation of keratinocytes, cell adhesion and migration, blood circulation, angiogenesis, and other immune reactions [68]. The flat-top handpiece 808-nm phototherapy with higher power and fluency promotes the

wound healing in the *Dendrobaena Veneta* earthworm through muscular contraction, which reduces the wound area, via inhibition of the inflammatory process demonstrated by the reduction of the coelomic plug and the non-cholinergic anti-acetylcholinesterase enzyme (AChE) production. In addition, by examining the macroscopical, histological, and immunohistochemical changes on the irradiated tail excised earthworms concerning controls [69].

3. Anatomical and biological properties of earthworm

Earthworm is an invertebrate that inhabits mainly in the top layer of the soil. Earthworms are classified as a genus by the scientific name *Pheretima*. Earthworms are reddish brown in color and have a cylindrical body. In addition, its body is elongated and pointed in the anterior region, with a rounded posterior region. A dark median mid-dorsal blood vessel can be found on the body's dorsal surface in (Figure 3-1). Genital openings or pores can be found on the body's ventral surface [70], [71].

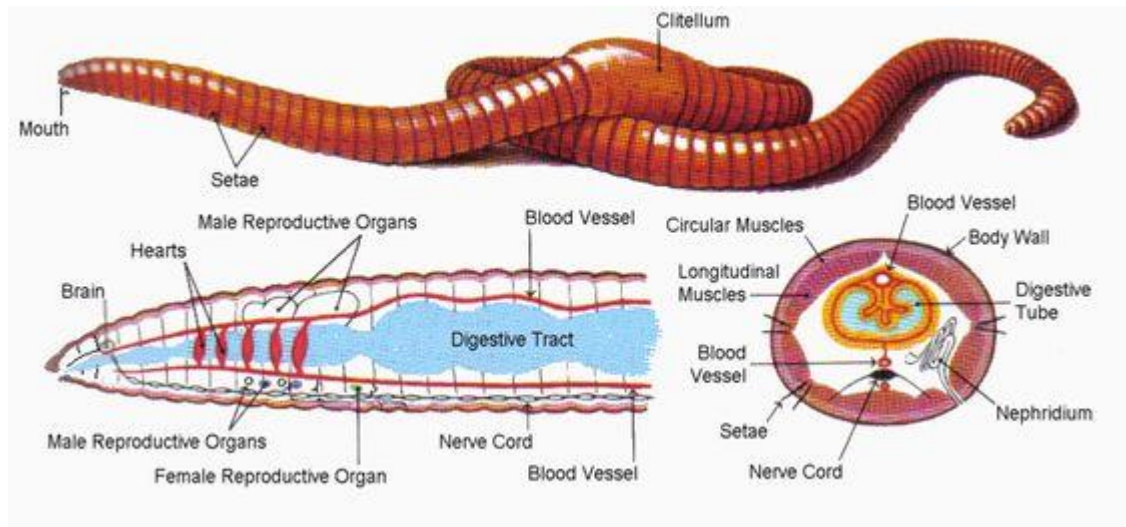


Figure 3-1. Homonyms segments of an *Eisenia andrei* earthworm. Longitudinal section of circular system. And anatomical cross section of earthworm [72].

Peristomium is the first body segment with a mouth. The anus can be found in the final segment. Furthermore, the clitellum is a prominent dark band of glandular tissue located between segments 14 and 16. On the body's surface, there are many small pores known as nephridiopores. Except for the first, last, and clitellum segments, all other segments have embedded S-shaped setae. These setae aid in locomotion.

The circulatory system contains of blood, blood vessels, capillaries, and heart. Because of the muscles contractions, blood flows in only one direction. The blood

glands, which produce blood cells and hemoglobin, are located in the 4th, 5th, and 6th segments. Blood cells lack hemoglobin and are phagocytic. It dissolves in blood plasma.

The excretory system is made up of coiled tubules known as nephridia. They are arranged on the body's segments. These nephridia are classified into three types based on their location. Septal nephridia, integumentary nephridia, and pharyngeal nephridia. They are responsible to maintain the volume of the body's fluids. Terrestrial oligochaetes have a limited number of specialized respiratory organs. The body surface is kept moist by the mucous glands of the epidermis dorsal pores, which exhibit coelomic fluid, and the nephridial excretions through the nephridiopores. This method of gas exchange is based on a network of small vessels embedded in the body wall of terrestrial earthworms, allowing oxygen dissolved in the surface moisture film to propagate through the cuticle and epidermis to the thin wall of these vessels [71], [72].

Alimentary canal is a straight tube that runs from the first to last segment of an earthworm's body. The mouth, which leads to the buccal cavity, is located in the anterior part of the body. This leads to the muscular pharynx, which is followed by the esophagus and the muscular gizzard. The muscular gizzard is a structure that aids in the abrasion of soil particles mixed with organic matter and depleted leaf particles. The gizzard connects to the stomach, which is present from the 9th to 14th segments [73].

On the ventral paired nerve cord, ganglia are arranged in a segmented manner. Each body segment has a ganglionic swelling of the cord. In the 3rd and 4th segments, the nerve cord bifurcates and laterally encircles the pharynx before joining the cerebral ganglia dorsally to form a nerve ring. This integrates sensory input, and controls the earthworm's muscular responses [74]. The cerebral ganglion was connected by a circumpharyngeal nerve to a nerve cord that laid ventrally.

Histology of earthworms body wall consists of a cuticle layer, an epidermis, a circular muscle layer, a longitudinal muscle layer, and a peritoneum, from outer to

inner layer [75]. The posterior setae swell up to keep the hind body in place, while the anterior circular muscles contracts, allowing the anterior portion to stretch forward. The typhlosole causes the intestine to fold in order to increase the absorption area. The ventral blood vessel transports blood from the anterior to the posterior parts of the body, as well as to the most organs, whereas the dorsal vessel transports blood in the opposite direction. The ventral blood vessel is smaller in diameter than dorsal vessel due to additional outer longitudinal muscle layer at lateral portion [76], [77], and coelomic cavity filled by coelomocytes in (Fig. 3-2).

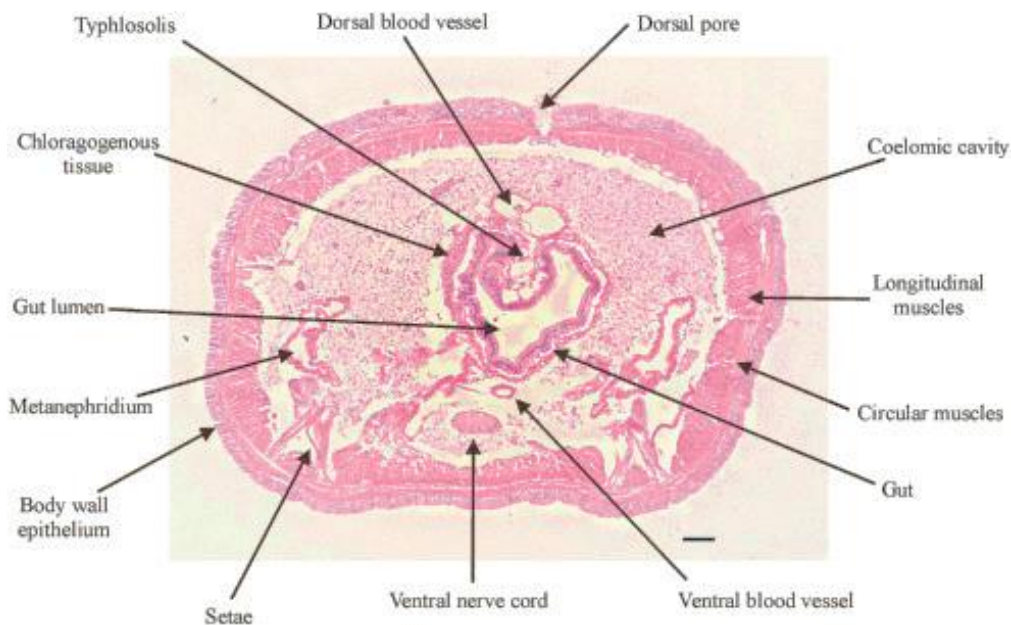


Figure 3-2. Cross section of an *Eisenia andrei* earthworm. Main organs and tissues are marked. Hematoxylin-eosin staining. Note that the coelomic cavity is filled with coelomocytes. Scale bar: 100 μm [78].

3.1. Regenerative capacity in animals

The replacement of body parts lost due to injury is a common definition of regeneration. Invertebrates of the *Planariidae* family and Hydra genus are at the top of this hierarchy, as they have the capacity to renew whole animals from tiny body pieces or even from small numbers of dissociated and reaggregated cells [24], [79]. The basis of regenerative differences between organisms is poorly understood. One possibility is

that some genes are present and functional in highly regenerative capacity animals but not in those that are not.

To date, evidence for this model has been reported for just a single gene: Prod1 was identified in a differential cDNA screen for sequences implicated in proximodistal identity in limb regeneration by newts. Prod1 is implicated in limb regeneration and seems to be a salamander specific gene that is not represented in fish or mammalian genomes [80], [81].

More research is needed, including functional studies and more precise comparisons with corresponding mammalian structures, but it's intriguing to speculate that regenerative capacity is at least in part a function of access to molecular programs typically used for adult growth and maintenance. There's a lot of interest right now in age-dependent regulators of regenerative capacity, and this area shows promise for future research [82].

3.2 Regenerative capacity of earthworm

The earthworm is a unique and valuable model for investigating the mechanism of regeneration, among all animal species, a few have the remarkable capacity to regenerate a missing part of their body following amputation. Earthworm regeneration could provide a unique and valuable model to investigate the mechanism of regeneration in that: 1. earthworm regeneration takes a relatively short period of time. *Eisenia Andrei* was used in this study can completely regenerate an amputated tail within 30-35 days post-amputation [83]; 2. in comparison to other animals, earthworm regeneration necessitates the reformation of distinct tissues or organs. The earthworm must regenerate its intestinal, cholagogues tissue (a hepatoid tissue of the earthworm), nephridia, setae, septa, and other structures in order to regenerate a complete tail; and 3. earthworm regeneration is bidirectional. It is thought that the earthworm is the highest evolutionary form capable of regenerating an anterior portion containing a brain, heart, and clitellum [84].

However, it has been reported that when the nerve cord was completely

removed, regeneration did not occur [85]. Moreover, when the anterior portion of an earthworm was amputated and the nerve cord removed from a few of the remaining segments, regeneration started at the segment that still had its nerve cord. These facts suggest that earthworm regeneration is controlled by the nervous system [86]. In addition, the regeneration of giant axons has been intensively investigated as a possible model to understand the mechanism of neuronal regeneration in other animals [87]–[89].

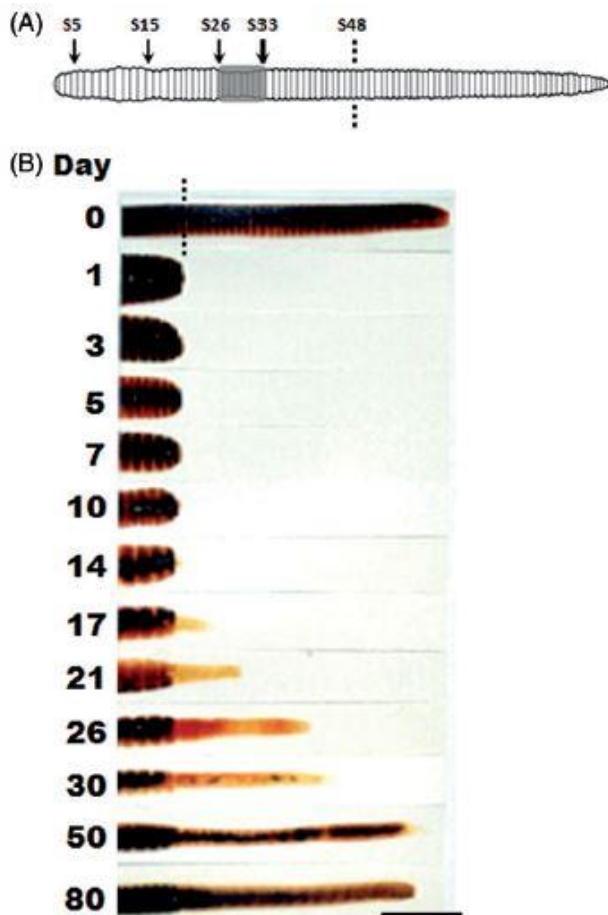


Figure 3-3. The process of tail regeneration in *E. Andrei* from day 1 to 80 days post-amputation. All earthworms are oriented in a lateral view with anterior to the left. (A) schematic of an adult earthworm indicating the amputation site at segment (S48). Adult earthworms have a distinct swelling called a clitellum, which extends from segment 26 to 33. (B) At 1 and 3 days, extrusion of intestine was observed, and wound healing was being processed. The outgrowth of regenerating tissue was observable from 14 to 17 days. At 21 days, segmentation of regenerating tail was seen. After 30 days, the growth of the regenerating tail was very rapid, followed by differentiated segments and pigmentation. Black dotted lines indicate an amputation site in all panels. Scale bars 1 cm (B) [90].

The epimorphic regeneration process, which involves dedifferentiation and cell proliferation, is a valuable model for studying the mechanisms of proper development and differentiation [90]. Park et al studied the developmental change in blastemal cells during earthworm tail regeneration in (Figure 3-3) [90].

For vertebrates such as amphibians, the formation of a blastema is known as epimorphic regeneration. The process of epimorphic regeneration involves dedifferentiation and cell proliferation, and provides a useful model to investigate the mechanism of normal development as well as differentiation [91]. The blastemal cells arise from myofibers [92], cartilage [93], the dermis [94], and nerve cells after amputation [95]. The remodeling of the extracellular matrix (ECM) triggers dedifferentiation, a change in cell type from fully differentiated to pluripotent [96]–[98]. On the other hand, planarians and hydra blastema cells are derived from pre-existing undifferentiated cells (neoblasts) that are widely distributed throughout their bodies, as opposed to the cellular dedifferentiation observed in vertebrates [99]. Furthermore, it is generally believed that the rearrangement of ECM is closely associated with the regulation of development and differentiation by enabling cell migration and cell-cell interactions and by regulating the release of sequestered growth factors [100]. There are several lines of evidence indicating that ECM-degrading proteinases secreted from stump cells and the blastema itself are responsible for the rearrangement [101]; [102].

However, the precise involvement of proteinases in dedifferentiation and blastema development, as well as the distinct roles of each proteinase, are unknown. As a result, at the tissue, cellular, and molecular levels, the earthworm's regeneration is poorly known. The results of this study in chapter 7 show that THz pulses stimulate the earthworm regenerated segments.

4. THz pulse generation and measurements

4.1. THz generation

4.1.1. Optical rectification and tilted pulse front

In powerful pulsed THz sources, lithium niobate (LiNbO₃, LN) is now the most widely utilized nonlinear material. As a result, its properties are being examined in more depth. It's also one of the most adaptable optical materials. Electro-optics, piezoelectricity, acoustic-opticity, photorefractiveness, pyro-electricity, and photovoltaicity, among other qualities, could be useful in applications. Optical waveguides, piezoelectric sensors, optical modulators, and a range of other linear and nonlinear optical components are all made from LN single crystals. In the mid-1960s, Bell Laboratories developed LN, a man-made ferroelectric crystal. It's a colorless solid that's insoluble in water. At wavelengths ranging from 0.35 to 5.2 μm, it is transparent. Its crystal system is trigonal [103].

LN is highly suited for optical rectification because to its substantial second-order nonlinear coefficient. However, because of the significantly differing optical group and THz refractive indices, the THz generation efficiency remains poor without extra steps. As the THz phase fronts spread through the crystal, the pump pulse overtakes them. It is evident that in a velocity-matched medium, a long crystal can be employed and a huge interaction length can be produced. Hebling et al. proposed tilting the intensity in front of the pump pulse to achieve velocity matching in LN [104]. The THz radiation that is excited by the tilted pulse front of the NIR pump propagates perpendicularly to this front with the velocity v_{THz} . The angle between the propagation direction of the THz and the direction of the pump pulse will be the same as the tilt angle γ of the pulse front relative to the phase front of the pump. The following equation holds in case of velocity matching:

$$v_{NIR}^{gr} \cos\gamma = v_{THz} . \quad (3)$$

If $v_{NIR}^{gr} \geq v_{THz}$ holds, v_{NIR}^{gr} is a group velocity of the pump beam, this modified velocity matching condition can be easily fulfilled by an appropriate choice of the angle γ . Pulse front tilting of a light beam necessarily leads to angular dispersion. The connection between the pulse front tilt γ and angular dispersion for material with refractive index n is given by [105]

$$\tan\gamma = -\frac{n}{n_{gr}} \lambda \frac{d\varepsilon}{d\lambda}. \quad (4)$$

Here, n is the refractive index, n_{gr} is the group refractive index, λ is the wavelength and $d\varepsilon/d\lambda$ is the angular dispersion, where:

$$n_{gr} = n - \lambda \frac{dn}{d\lambda}. \quad (5)$$

Optical rectification of ultrashort laser pulses with tilted pulse front in LN [104] has been implemented as a reference technique for efficient THz generation. In THz generation experiments, perpendicular pump coupling and perpendicular THz beam outcoupling are the conditions for minimizing reflection losses and avoiding angular dispersion of the THz beam. As a result, a prism-shaped LN crystal with a large wedge angle equal to the pulse-front tilt is used (63°). The illustration of velocity matching using tilted-pulse-front is depicted in Fig. 4-1.

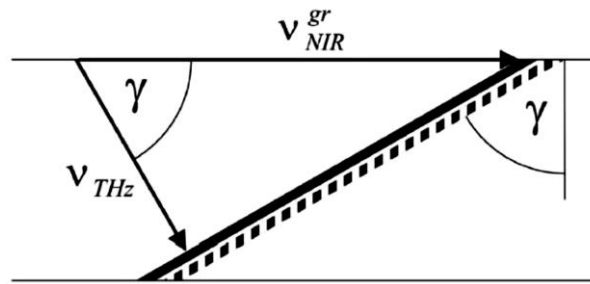


Figure 4-1. Illustration of velocity matching using tilted-pulse-front [106].

Fig. 4-2 shows the pulse-front-tilting setup and its parameters, θ_i , and θ_d are incidence and diffraction angle at the grating, respectively. θ_d also gives the tilt angle of the grating. The distance S between the image of the grating and the crystal input surface along the optical axis. The S is arbitrarily chosen so that the region of effective

THz generation is not truncated. The geometrical parameters of the setup in Fig. 4-2 [107].

$$\sin\theta_d = \frac{\lambda_0}{n(\lambda_0)n_{gr}(\lambda_0)p} a \quad (6)$$

$$\sin\theta_i = \lambda_0/p - \sin\theta_d \quad (7)$$

$$S_1 = f(\sqrt{a}+1) \quad (8)$$

$$S_2 = \frac{fS_1}{S_1-f} - \frac{S}{n(\lambda_0)} \quad (9)$$

Where, λ_0 is the central wavelength, p is the grating period, f is the focal length of the lens, a is a constant,

$$a = \frac{n^2(\lambda_0)n_g(\lambda_0)p}{2\lambda_0} \sqrt{\frac{\lambda_0^2}{n_g^2(\lambda_0)p^2 \tan^4\gamma} + \frac{4}{n^2(\lambda_0)} - \frac{n^2(\lambda_0)}{2\tan^2\gamma}} \quad (10)$$

Where λ_0 is the pump beam wavelength, p is the grating period, f is the focal length of lens, S can be chosen according to the spot size and it is typically 1 – 5 mm. To achieve optimal pump-to-THz conversion and THz beam characteristics, the setup should meet the following criteria: Pump pulse and THz velocity matching, pump pulse duration has to be minimal across the tilted pulse front, and pump pulse front must be plane in the crystal [107].

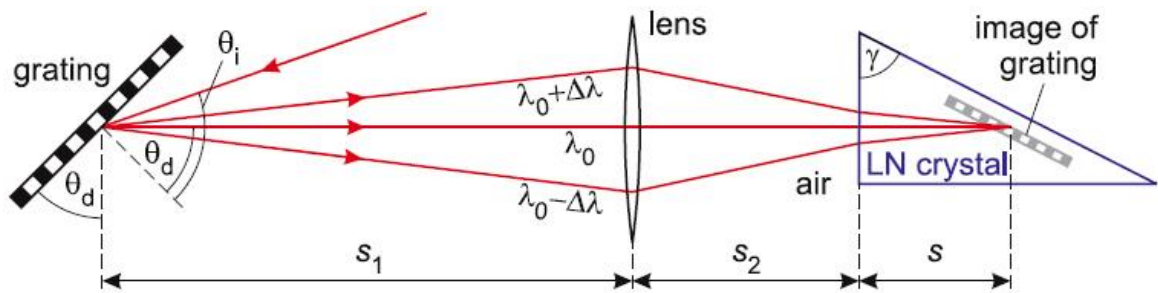


Figure 4-2. Tilted-pulse-front-pumping setup [108].

Since the diffraction efficiency of a grating is usually maximal in Littrow-geometry, using an incidence angle close to the Littrow-angle $\theta_{Littrow} = \sin^{-1}(\lambda_0/2p)$ will be advantageous. Attempting to increase THz energy in tilted-pulse-front pumping scheme by increasing pump energy and spot size has some limitations. A prism-shaped

LN crystal with a large wedge angle equal to the pulse–front tilt (63°) results in a non-uniform pump propagation length across the beam. Such a source geometry can result in a spatially varying interaction length for THz generation [108]. Several approaches have been proposed to reduce the tilted-pulse-front pumped THz source's limitations.

4.1.2. Photoconductive antennas

Another widely used technique for the generation and detection of both pulsed broadband and single frequency continuous-wave THz band radiation is the photoconductive antenna (PCA). In this technique, an ultrafast femtosecond laser interacts with a biased photoconductive semiconductor with a carrier lifetime of sub-picosecond (low-temperature-grown GaAs, LT-GaAs), resulting in a transient photocurrent. The transient photocurrent with a pulse width of sub-picosecond, radiates an electromagnetic wave in the THz spectrum [109].

Many efforts have been made to improve laser pulse coupling into LT-GaAs substrates and improve PCA performance, including the use of antireflection coating on LT-GaAs substrates, three-dimensional nanoplasmonic structures, double-layer nanoplasmonic structures, optical plasmonic nanoantennas, and others. Most of these methods actually require electron beam lithography which raises the cost and time of fabrication significantly [110]–[115].

4.2. THz pulses characteristics and measurements

4.2.1. Power/Energy measurements

THz radiation is typically detected using thermal detectors. A THz radiation absorber contacted to a heat sink is the basic component of thermal sensors. The thermal absorber converts the absorbed radiation energy into heat, and a thermometer component measures the temperature changes caused by THz. Pyroelectric crystals are spontaneously polarized crystals with a permanent electric dipole moment aligned with a specific crystal axis in each unit cell [46]. The magnitude of this spontaneous

electric polarization varies with temperature. The spontaneous polarization is followed by surface charge, which is neutralized by free carriers, resulting in a steady state.

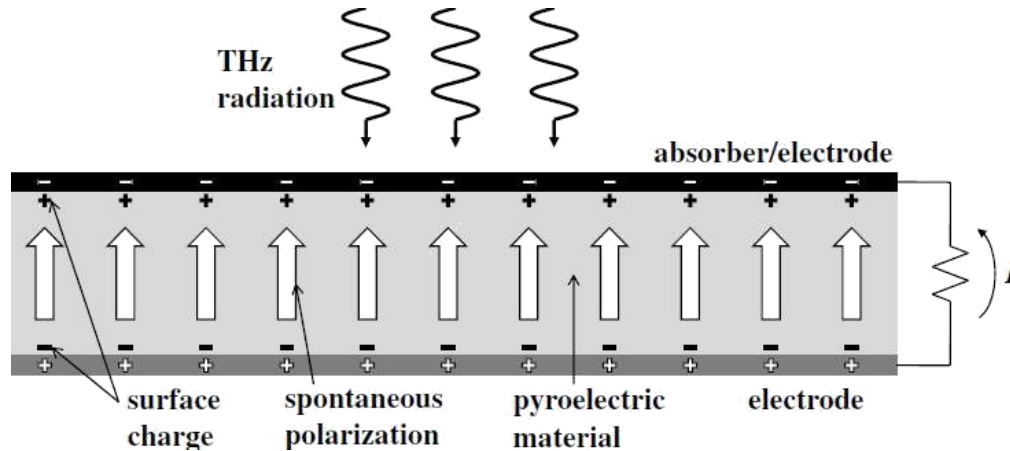


Figure 4-3. Schematic diagram of a typical pyroelectric detector [46].

Fig. 4-3 shows the basic scheme of a pyroelectric detector. The pyroelectric crystal is sandwiched between two electrodes, one of which is typically treated to absorb incident radiation. The heat generated by the radiation raises the temperature of the pyroelectric crystal, causing a decrease in spontaneous polarization and surface charge. The attached electrodes on the two opposite crystal surfaces form a capacitor [46].

4.2.2. Electro-optic sampling

Valdmanis et al. have previously reported on electro-optic (EO) sampling for the characterization of ultrafast electrical transients. The technique is unique among sampling systems because it is based on an electric field coupling between the electrooptic “sampling gate” and the circuit [116]. The electric field of THz pulses is measured in the time domain using free-space electro-optic sampling, which determines not only the amplitude but also the phase. The Pockels effect is at the heart of electro-optic sampling [117].

The electro-optic effect is primarily a nonlinear coupling of an electric field (THz pulse), and a laser beam (optical pulse) in the sensor crystal. The Pockels effect is related to optical rectification, as evidenced by the similarity of their second-order nonlinear polarization expressions:

$$\begin{aligned}
P_i^{(2)}(\omega) &= 2 \sum_{j,k} \epsilon_0 X_{i,j,k}^{(2)}(\omega, \omega, 0) E_j(\omega) E_k(0) \\
&= \sum_j \epsilon_0 X_{i,j}^{(2)}(\omega) E_j(\omega),
\end{aligned} \tag{11}$$

where, $X_{i,j}^{(2)}(\omega) = 2 \sum_k \epsilon_0 X_{i,j,k}^{(2)}(\omega, \omega, 0) E_k(0)$ is the field induced susceptibility. In a lossless medium $X_{i,j,k}^{(2)}(0, \omega, -\omega) = X_{i,j,k}^{(2)}(\omega, \omega, 0)$, thus the Pockels effect has the same nonlinear optical coefficients as optical rectification. Eq. (11) indicates that a static electric field creates birefringence in a nonlinear optical medium in proportion to the applied field amplitude. Inversely, the applied field strength can be determined by measuring the field-induced birefringence [118].

Fig. 4-4 illustrates a typical free-space EO sampling setup for measuring field-induced birefringence. The change of the probe's polarization is shown in a series of polarization manipulation steps with and without a THz field. Although both the linearly polarized optical pulse and the THz pulse propagate through the EO crystal, the polarization of the probe pulse is a little elliptical due to field-induced birefringence. After $\lambda/4$ plate, the probe polarization evolved into a roughly circular, but elliptical polarization. The probe beam is split into two orthogonal components by a Wollaston prism, which is then sent to a balanced photodetector. The detector measures the intensity difference $I_s = I_x - I_y$ between the two orthogonal components of the probe pulse, which is proportional to the applied THz field amplitude [46].

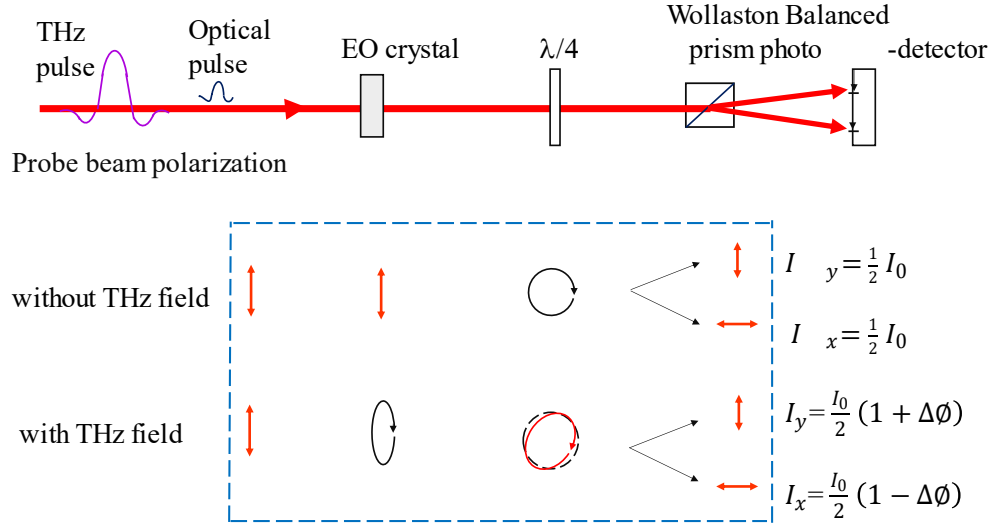


Figure 4-4. Schematic diagram of a typical setup for electro-optic sampling [118].

Zinc-blende crystals such as ZnTe or GaP are often used for electro-optic sampling. The useful characteristics of ZnTe crystal for THz generation (like high transparency at optical and THz frequencies, large electro-optical coefficient) are also desirable for efficient electro-optic sampling. ZnTe is also suitable, because its far-infrared refractive index is comparable to the near-infrared index, contributing to reasonably efficient detection of THz [119].

4.2.3. Time-domain THz spectroscopy

THz radiation is used in time-domain terahertz spectroscopy (TDS), which is a spectroscopic technique for probing the characteristics of materials. The essential concept behind TDS is that the electric field of a THz pulse is measured as a function of time. If the THz pulse passes through a material (a biological tissue in this investigation), its time profile gets changed compared to the reference pulse. The reference pulse can be a pulse propagating in vacuum or a medium with known properties. By comparing the THz pulse transmitted through the medium with the reference THz pulse we can find the changes introduced by the material

[120]. A basic Fourier transformation can obtain both the amplitude and phase of the spectral components from a waveform because it contains all of the information. This enables the measurement of a sample's absorption and dispersion properties at the same time [118].



5. Infrared and green optical pulses

5.1. Infrared pulses from an Yb laser

Yb^{3+} is an attractive luminescent ion for high power laser applications because it has a quasi 4-level structure that limits loss from cross relaxation and/or up-conversion. Yb^{3+} also has broad absorption and emission bands that facilitate diode pumping as well as short pulse generation and laser wavelength tunability [121].

One high-efficiency Yb-based laser material for broadband high average-power is Yb-doped potassium gadolinium tungstate crystals (Yb:KGW). The large spectral width of Ytterbium (Yb) in crystalline hosts permits a direct diode-pumped solid-state (DPSS) laser operation in the femtosecond regime [122].

Another laser crystal used in regenerative amplifier is Yb:CaF₂. The coordination of Yb^{3+} in the CaF₂ lattice determines the spectroscopic properties that make Yb:CaF₂ a good candidate for high power laser applications [123]. Recent studies have demonstrated single crystal Yb:CaF₂ laser gain media with 50% slope efficiency [124], generation of 150 fs laser pulses [125], and internal-Q-switching [126]. Single crystal Yb:CaF₂ also exhibits a higher damage threshold compared to single crystal Yb:YAG (52 J cm⁻² and 16 J cm⁻², respectively, for a 10 ns pulse duration at a center wavelength of 1064 nm) [127]. Yb^{3+} dopes into the CaF₂ structure by substituting for a Ca²⁺ on the cation sublattice and creating a charge compensating F⁻ interstitial on the anion sublattice. Hexamer clusters have been subsequently identified in single crystal

Yb:CaF₂ as the primary luminescent centers, and the energy manifolds of these hexamer structures are critical to the attractive laser gain properties of Yb:CaF₂ [128].

In the present study, two different Yb-based laser systems were used. One of them was a commercial Yb:KGW regenerative amplifier from Light Conversion, which delivered 1-mJ, 180-fs pulses at 1 kHz repetition rate. The other system was a custom-made cryogenically cooled Yb:CaF₂ regenerative amplifier from Amplight KG., delivering 7-mJ, 200-fs pulses at 1 kHz repetition rate.

5.2. Second harmonic generation (green light)

High power sources of visible (green) and ultraviolet ultrashort laser pulses are attractive for an oversized number of scientific and technical applications like spectroscopy, laser projection displays, or micromachining [129]. Frequency doubling (SHG), tripling (THG), or quadrupling (FHG) of ultrafast laser sources with near-IR wavelengths produces these pulses. Other nonlinear optical frequency extension devices, such as optical parametric devices, can be pumped with the ultrashort pulses in the green wavelength. Second harmonic generation (SHG; also known as frequency doubling) is a process in which the basic laser wavelength is frequency doubled, i.e. the wavelength becomes half of its fundamental value, by passing it through a nonlinear crystal. The nonlinear material efficiently combines two incident photons of same energy to a new photon of twice the energy. The optical response of a material can be written as

$$\vec{P} = \epsilon_0 \chi \vec{E} \quad (12)$$

where, χ is the susceptibility tensor, \vec{P} is the polarization vector and \vec{E} is the electric field vector.

In this study a Beta Barium Borate (BBO) crystal has been used, as the nonlinear material, for the conversion of the 1030-nm infrared light of a Yb-based laser

sources to green light with 515 nm wavelength. The second harmonic generation was performed in a single-pass geometry using a BBO crystal for type-I critical phase matching. The BBO crystal of 2 mm thickness had antireflection coating for both the fundamental, and the second-harmonic wavelengths.

6. Scientific goal

Terahertz pulse applications are versatile and abundant. The interaction of THz radiation with living systems is often an extremely complex process and is the basis for important applications in THz imaging and spectroscopy of living matter. In this study, the aim was to systematically study the effect of non-ionizing electromagnetic radiation of THz pulses on biological cells. The main goal was to deliver fundamental new information on the influence of intense pulsed THz radiation on cells in a tissue, which may be useful later in medical applications and veterinary.

The first goal of this study was to compare the effects of intense single-cycle THz pulses on earthworm regeneration capacity after excision with worms that were not irradiated with THz pulses. THz pulses significantly improve cell division during the mitosis phase of the cell cycle. It helps to differentiate epithelial, muscle, endothelial, and neural tissues in certain parts of the *Eisenia andrei* earthworm. Furthermore, after the cut, the effects of THz pulses were compared on the capacity of regenerated segments with visible green light.

Another goal of this study was to characterize the interaction mechanism of THz pulses with biological tissues. Therefore, the transmitted THz pulses were measured on isolated tissues. The transmission of near-infrared and green laser pulses was compared to that of THz pulses in various tissue thicknesses. Isolated tissues in the animal model used in this study contain approximately 82% water molecules, making water the major absorber of THz radiation. The aim was to estimate, by a simple numerical model, the amount of heat transferred to the tissues by irradiation of THz pulses with 5 μ J energy and 1 kHz repetition rate (5 mW average power).

The third goal of this study was to determine the absorption coefficient of the THz pulses in tissues by time-domain THz spectroscopy. To calculate the tissue's optical properties, it is necessary to reconstruct its optical parameters from the measured transmission spectra [130].



7. Results

7.1. Terahertz pulses induce segment renewal of the earthworm *Eisenia andrei*

7.1.1. Experimental animals

In all experiments healthy, sexually matured (clitellated) specimens of the earthworm *Eisenia andrei* (Annelida, Oligochaeta, Lumbricidae) were used which were handsorted from the breeding stocks maintained at standard laboratory conditions as described earlier [131]. The selected specimens were kept on wetted paper wadding for three days to remove gut content. For species identification the mitochondrially encoded cytochrome c oxidase I (MT-CO1) gene sequestration was used [132].

7.1.2. Ablation of tail segments

A standard method developed in our laboratory was used to excise the specimens [18]. The purified animals were anaesthetized with carbonated water at 4 °C to total movelessness and insensitivity. By the aid of a stereomicroscope 25 posteriormost segments were counted and ablated with quick, sharp scissors cutting at the segment furrow (Fig. 7-1). The quality of the surgical interventions (wholeness of the last segment located before the cutting) was immediately inspected and only those animals were introduced into the experiments in which the segment boundary (dissepiment) was intact.

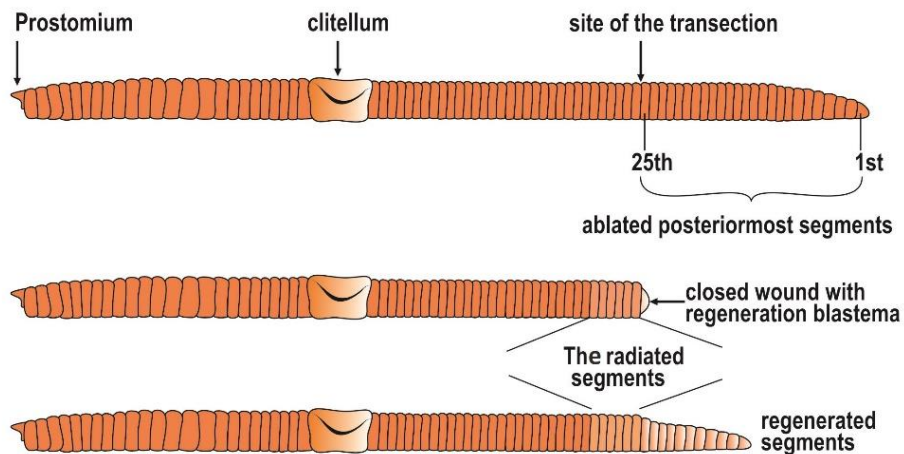


Figure 7-1. Flowchart of the tail segments removal and regeneration in the earthworm showing the THz radiated body part.

7.1.3. Further handling and experimental treatment of worms

Immediately after the segment ablation, the animals were distributed into three groups, each with 15 specimens, and kept at room temperature (24 °C) in garden compost wetted with tap water. Group C was the control (sham-exposed), group T received purely THz irradiation, and group G was exposed to green light (second harmonic of the infrared laser light). Before the irradiation, worms of all groups were selected from the compost and anesthetized as described above. Then the worms were laid on a glass holder and placed on the exposition field of the equipment (Fig. 7-2). Four or five of their posteriormost segments were irradiated for 5 minutes at the end of the first postoperative hour. The irradiation was repeated on the first and second postoperative days. The control animals were handled similarly to the irradiated ones (including anesthesia), except the exposition to radiation, and they were kept in a plastic holder at room temperature. Immediately after the treatment, the animals were introduced into the mixture of compost and soil. The number of regenerated segments was counted from the 2nd postoperative week to the 4th one with a stereomicroscope.

7.1.4 Characteristics of the applied irradiation pulses

7.1.4.1. THz pulses

The irradiation setup is shown in (Fig. 7-2). For THz irradiation, the components within the green box were removed from the setup. Single-cycle THz pulses were generated by optical rectification of short infrared laser pulses in LiNbO₃ (LN) crystal using the tilted-pulse-front technique [104], as shown in (Fig. 7-2). The infrared pump pulses of 1030 nm central wavelength, 200 fs pulse duration, and up to 7 mJ energy were delivered by an Yb:CaF₂ regenerative amplifier at 1 kHz repetition rate. The THz source and its characterization are described in more detail in an earlier study [133]. Briefly, the laser pulse was diffracted off a grating to introduce a pulse-front tilt and imaged from the grating into the LN prism. The generated THz pulses leaving the prism were collimated and focused onto the sample by a pair of off-axis parabolic mirrors with effective focal lengths of 4 and 3 inches (Fig. 7-2). A Teflon filter between the two parabolic mirrors was used to stop any possible scattered or transmitted optical radiation to reach the sample.

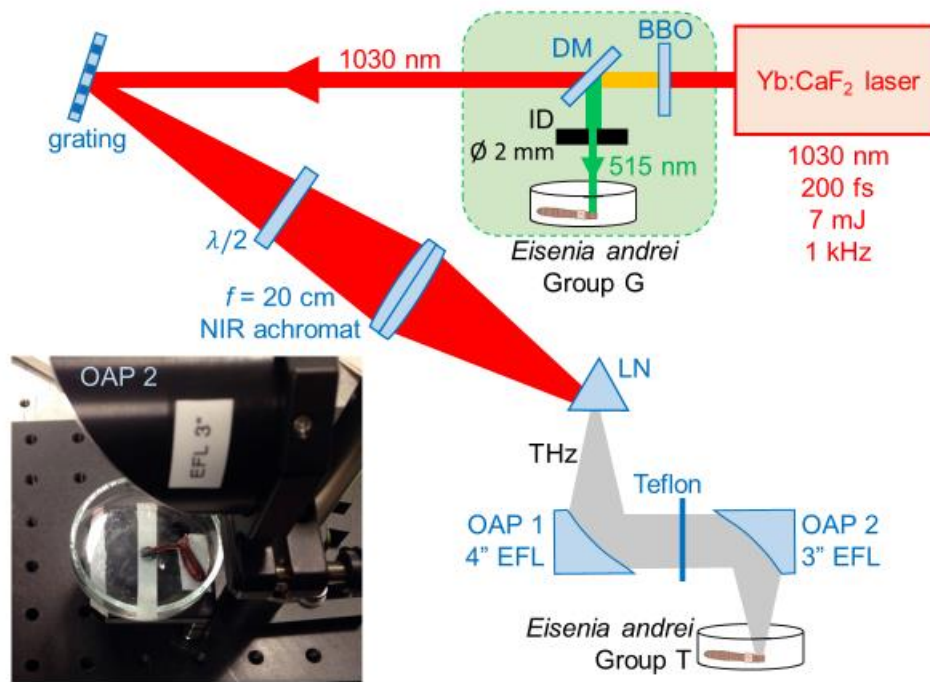


Figure 7-2. Scheme of the irradiation setup. The *E. andrei* specimens of Group G were placed into the green laser beam. The specimens of Group T were placed into the focus of the THz beam. In this case the components within the green box were removed from the setup. DM: dichroic mirror, $\lambda/2$: half-wave retardation plate, OAP: off-axis parabolic mirror, EFL: effective focal length. The bottom left inset shows a photograph of an anaesthetized earthworm at the THz irradiation position.

The THz intensity distribution in the focus was measured by a pyroelectric camera (Ophir, model Pyrocam IV). The diameters of the slightly elliptical focal spot were $2w_x \times 2w_y = 2.14 \text{ mm} \times 2.54 \text{ mm}$ (full widths at $1/e^2$ of the peak intensity, Fig. 7-3(a)). The waveform of the THz pulses was measured by electro-optic sampling and exhibits a single oscillation cycle (Fig. 7-3(b)). The measured THz pulse energy ($W = 5.0 \mu\text{J}$), the focal spot size, and the waveform were used to calibrate the peak electric field strength being about $E_0 = 293 \text{ kV/cm}$ at the beam center. The corresponding peak fluence was $F_0 = W/(w_x w_y \pi/2) = 234 \mu\text{J/cm}^2$ (assuming Gaussian intensity distribution) and the peak instantaneous intensity $I_0 = \epsilon_0 c E_0^2 = 229 \text{ MW/cm}^2$. Here, ϵ_0 is the permittivity of free space and c is the speed of light in vacuum. Fourier transformation of the temporal waveform gives the amplitude spectrum $A(\nu)$ (inset in Fig. 7-3(b)). A

mean frequency of $\bar{\nu} = 0.30$ THz was calculated from the spectral intensity $A^2(\nu)$ according to $\bar{\nu} = \int_0^\infty \nu A^2(\nu) d\nu / \int_0^\infty A^2(\nu) d\nu$. This frequency corresponds to an oscillation cycle of $1/\bar{\nu} = 3.3$ ps (the approximate pulse duration of the single-cycle waveform). The average intensity over the oscillation cycle was $\bar{I} = F_0 \bar{\nu} = 70$ MW/cm² at the beam center.

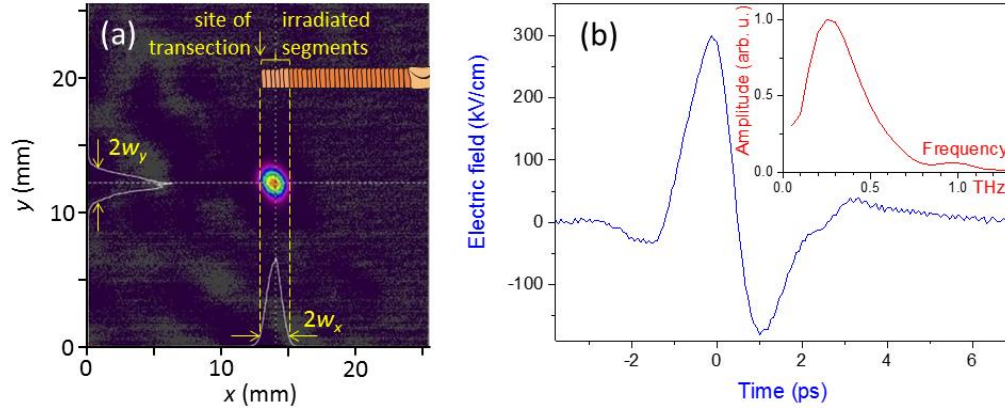


Figure 7-3. (a) Image of the THz beam spot at the sample location. The inset in the top right shows in side view the nominal position of the *Eisenia andrei* sample along the x direction. (b) Measured temporal dependence of the THz electric field. The inset shows the amplitude spectrum calculated by Fourier transformation of the waveform.

Special care was taken to precisely determine the beam location in the focal plane and to position the ablated tail part of the animals with the highest possible accuracy relative to the beam. The uncertainty in the animal positioning was about ± 0.5 mm, giving an estimated uncertainty in the effective sample irradiation of about 15%. This value was obtained by integrating the two-dimensional Gaussian intensity distribution for a sample animal displaced by ± 0.5 mm from the nominal position, where the site of transection was at $1/e^2$ of the peak intensity (inset in Fig. 7-3(a), see also Section 2.3) Because the root-mean-square energy fluctuation of the THz pulses was about 1%, the main source of uncertainty in the irradiation level was the uncertainty in animal positioning. Similar was the case with the green light irradiation (see Section 7.2.2).

7.1.4.2. Green light

Group G, with 15 amputated *E. andrei* earthworms, was exposed to green light. This was produced by phase-matched second-harmonic generation of the infrared laser pulses in a BBO crystal (Fig. 7-2). The beam diameter was adjusted by an iris diaphragm to 2 mm and the pulse energy was set to 5 μ J (the same as that of the THz pulses). A dichroic mirror, transmitting the infrared and reflecting the green, was used to separate the two wavelengths.

7.1.5. Regeneration blastema formation and kinetics of segment regeneration

The wound closure, regeneration blastema, and renewing segment formation was studied with both anatomical and histological methods on the sixth postoperative hour, and further on weekly till the fourth postoperative week. The earliest unambiguous identification of the regenerating segments was possible based on the strip-like accumulation of yellow-colored coelomocytes in the forming coelomic sacs on the first postoperative week. Later on, segment boundaries were already clearly seen because of the segmental organization of the circular muscles of the body wall (Fig. 7-4). Because of the triplicate repetition of the experiments the average segment number was calculated based on the investigation of 3x15 animals from each group.

7.1.6. Histological investigations

The time course of the regeneration was investigated on the 6th postoperative hours and on weekly from the 1st to the 4th postoperative periods. From anaesthetized animals (5 from each group) the regenerating body parts with 3 or 4 original segments were dissected and fixed in freshly prepared formalin-acetic acid solution (6 ml 38% formalin, 1 ml cc. acetic acid, and 18 ml distilled water), developed in our laboratory, for 72 hours at room temperature. Prolonged fixation for 2 weeks did not influence the staining properties of the sections. The fixed samples were washed and embedded into Paraplast Xtra (Merck Group, Hungary) as usual. Serial sections with 10 μ m were cut with a rotary microtome and attached to gelatin coated slides and stained with

Mayer's hematoxylin and eosin according to the conventional microtechnical protocols [134]. After dehydration and clearing with xylene, sections were coverslipped by DPX mountant, then investigated by a Nikon Optiphot-2 photomicroscope.

7.1.7. Calculation of the mitotic index (MI) characteristic for distinct body parts

The number of interphase nuclei and mitotic figures (pro-, meta-, ana-, and telophase) was counted in 10 consecutive high power fields (400-fold magnification) of distinct parts of both original and regenerating segments of group C (sham-exposed), group G and T animals, respectively. The mitotic cells were identified based on their cytological characteristics. In nuclear aggregates, the presence of the definite filamentous projections of chromatin (chromosomes) was observed. The chromosome clumps of both ana- and telophase were counted as one mitotic figure. For calculation of the MI, the following formula was used:

$$MI = \frac{P+M+A+T}{N} \cdot 100\%. \quad (13)$$

Here, (P+M+A+T) is the sum of all cells in mitotic phase as prophase, metaphase, anaphase, and telophase, respectively, and N is the total number of cells counted. Apoptotic cells (having strongly condensed chromatin and cytoplasm) were clearly distinguished and they were not counted.

7.1.8. Statistics

Statistical analysis was performed with a computerized statistical package (SPSS). Results were presented as mean and all error bars represented the standard error of the mean. The effect of treatments was analyzed statistically by Student's t-test (means: paired, tow-sample equal variance) $p < 0.01$, and $p < 0.05$ were denoted as statistically significant.

7.1.9. Experimental results

7.1.9.1. Wound closure and formation of the regeneration blastema

Immediately after the body transection, the body wall muscles contracted and tended to the midgut forming a transient barrier to prevent the loss of the coelomic fluid and the blood. On the first postoperative day, the body wall tissues closely attached to the midgut, and a small circular regeneration blastema (cicatrix) formed between the body wall and midgut tissues (Fig. 7-4). The histological observations revealed that intense dedifferentiation of the epithelial and muscle layers of both the body wall and midgut contributed to the formation of scar tissues consisting mainly of dedifferentiated epithelial and muscle cells, however, few coelomocytes were also dispersed in it (not shown).

No difference was found in the kinetics of the wound closure and histological organization of the regeneration blastema between the control and the irradiated groups. The formation of the regeneration blastema, from which new segments arose, started close to the cut stump of the ventral nerve cord, where small basophil cells with high nucleus-cytoplasm ratio concentrated, which were identified as mesodermal stem cells (neoblasts) thought to be key players in regeneration (not shown).

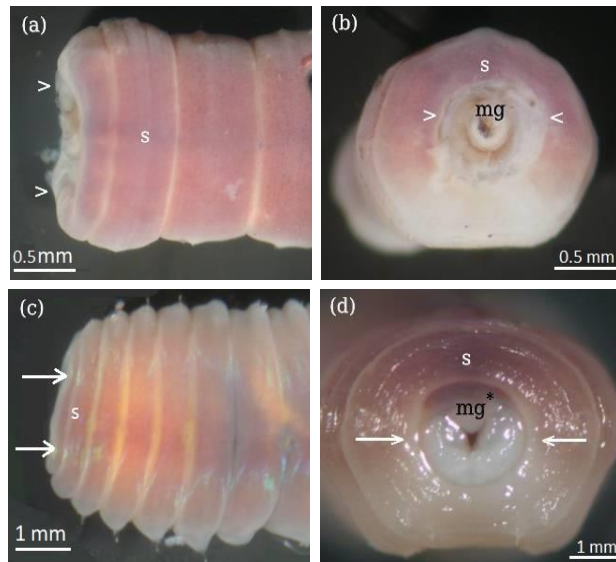


Figure 7-4. Anatomical characteristics of the segments in freshly operated animals (a,b), and in the sixth postoperative hour (c,d). Note that in the freshly cut segment, a quick contraction of the body wall can be seen, whereas, in the sixth postoperative hour, the fusion of the body wall and the midgut can be observed, forming a new internal opening. Abbreviations: mg - midgut, mg* - midgut is covered by thin layer of blast cells, s - segment, arrow heads label contracting body wall in (a,b), the arrow lines label the fusion of the tissues of body wall and midgut(c,d).

7.1.9.2. Kinetics of segment regeneration

The first renewed segments were clearly seen by a stereomicroscope after the first postoperative week (Fig. 7-5(a,c)), however their size extremely varied from animal to animal, and their number could not be definitely determined. In contrast to the first postoperative week, from the second week on, each regenerating segment was unambiguously identifiable. Therefore, the kinetics of segment regeneration of distinct experimental groups was compared from this point of time.

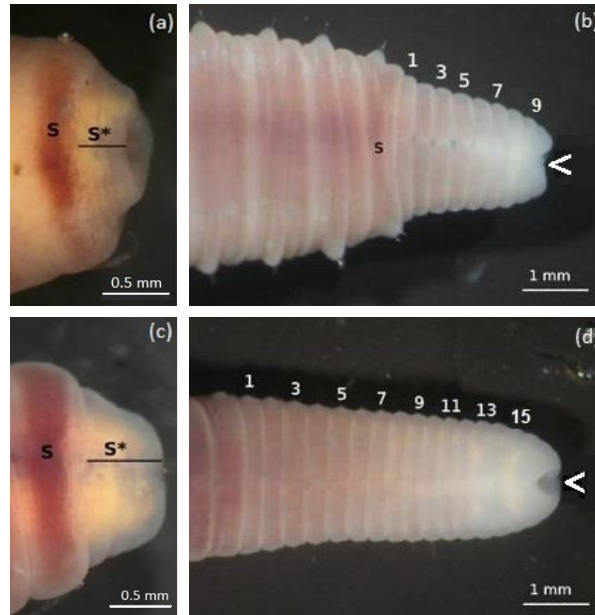


Figure 7-5. Comparison of the regenerated segment number of the control group (a,b) and THz-irradiated group (c,d) worms on the 7th (a,c) and on the 21st (b,d) postoperative day. Abbreviations: s - operated segment, s* - regenerating segments on the first postoperative week, Arabic numerals - regenerating segments on the third postoperative week, arrowheads – anus.

A huge difference in the regenerated segment number was found between the distinct groups of the experimental animals. Whereas THz pulses significantly stimulated the formation of the new segments, the green light did not have any influence on segment regeneration, indicated by nearly equal segment numbers to those in the control group (Fig. 7-6). The trend of the segment regeneration was the same on the third and fourth postoperative weeks, with about three times higher regenerated segment numbers in the THz-exposed animals than in green-exposed and control ones.

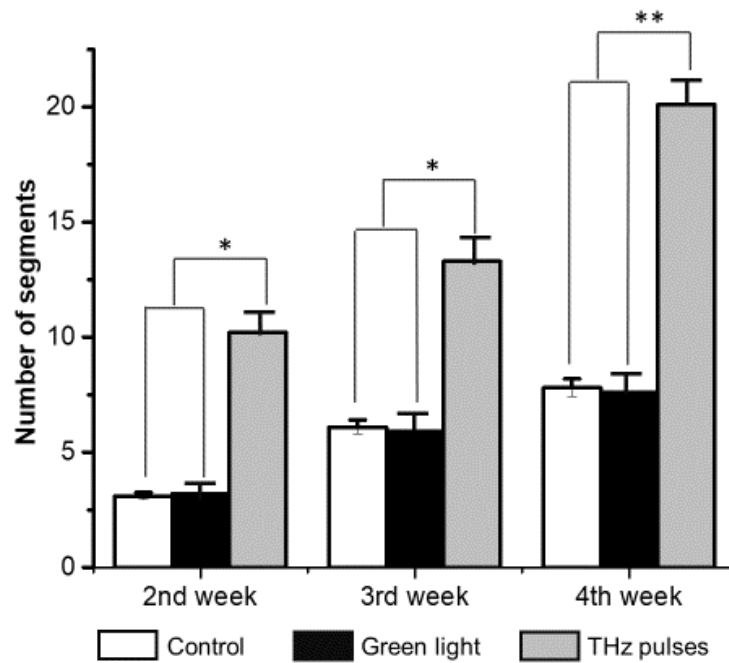


Figure 7- 6. Kinetics of the segment regeneration in control (sham-exposed) and green light or THz irradiated *E. andrei* earthworms. Data represent mean \pm SEM (n=45, *: p < 0.05, **: p < 0.01).

7.1.9.3. Histological characteristics of the regenerated segments in control and THz-exposed earthworms in the second postoperative week

Since renewing segments were unambiguously distinguishable on the second postoperative week and the intense segment formation also started at this time, the histological observations were focused on the 2nd week of the regeneration. The basic histological characteristics of the regenerated segments in group C (sham-exposed), group G (green light exposed) and T (THz exposed) worms were the same. Namely, the ventral part of the regenerated segments, connected to the old segment containing the ventral nerve cord (VNC), was significantly better differentiated than their dorsal parts. The formation of renewing segments could easily be identified based on the differentiating segment boundaries (dissepiments), whereas in renewing dorsal parts no segment differentiation was seen. The differentiation of the ventral nerve cord ganglia was faster than the differentiation of the body wall and the alimentary canal tissues.

Whereas group C and G animals showed the same histological characteristics, there were some marked histological alterations in THz-exposed specimens on the 14th postoperative day. In both the group C and G animals, the differentiation of the renewing body wall and VNC ganglia was on a smaller scale than in the T group because not only thinner but also less differentiated VNC ganglia and body wall were characteristic of the group C and G worms (Fig. 7-7(a,b)). In about 60% of THz-exposed worms, marked development of the blood vessels was seen in the regenerating segments, and in adjacent tissues of the blood capillaries, a high number of mitotic cells was located while in the residual ones advanced formation of the blood vessels, extension, and differentiation of various cells could be seen. No similar extension of blood vessels was characteristic of group C and G specimens on the 14th postoperative day (Fig. 7-7(c-e)).

Comparing the mitotic index of the distinct body parts of experimental animals marked results were collected from the specimens of groups of C, G, and T on the 14th postoperative day. Animals of groups of C and G were characterized by a higher MI (0.01) of all renewing structures (body wall and VNC ganglia) than of old ones (MI = 0.002). In specimens of group T, the MI of all newly formed organs proved to be significantly higher than in groups of C and G ones. For example, the MI of the regenerating VNC ganglia was 0.1, showing intense cell proliferation in these structures. Nearby the newly formed ganglia, several mitotic cells were located in the body wall, alimentary canal, and dissepiments (Fig. 7-7(d,e)). This conspicuous histological alteration was only found in about 40% of THz-exposed animals at the investigated period, while in others more advanced differentiation of tissues was observed. The smaller, less differentiated regenerating dorsal body parts, which was directly exposed to THz pulses, contained markedly higher number of mitotic figures (MI = 0.2) than the ventral ones (MI = 0.1), characterized by more extended and developed tissues and organs (Fig. 7-7(c)).

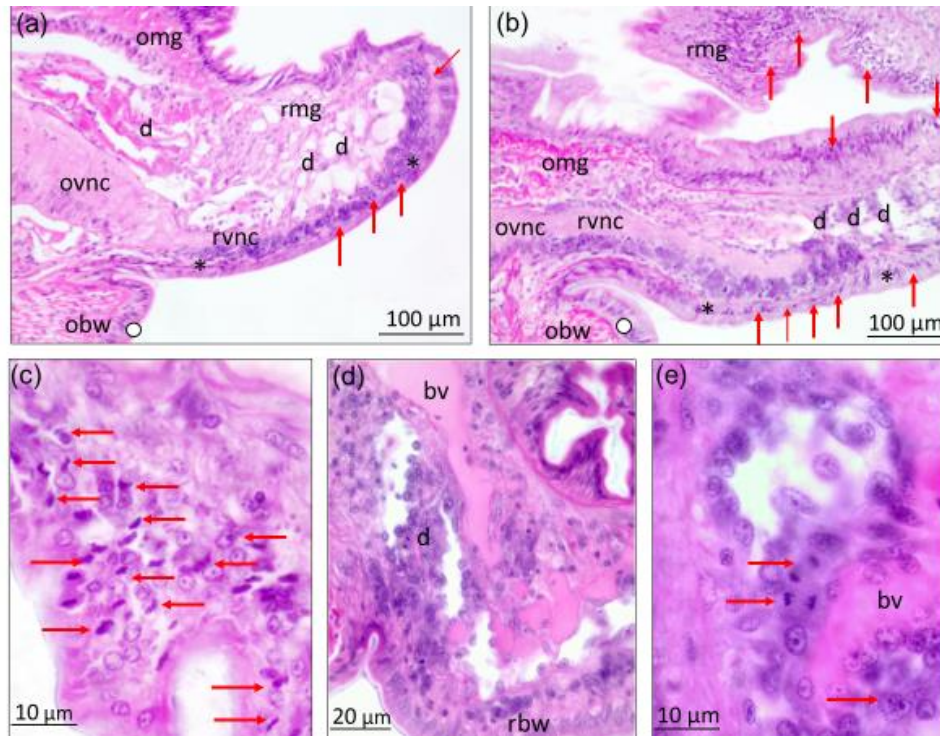


Figure 7-7. Histological characteristics of the regenerated segments of control (a), and THz-irradiated earthworms (b-e) on the 14th postoperative day. Since group G animals are characterized by the same histological alterations than group C ones their sections are not presented in the figure. Abbreviations: ovnc: old ventral nerve cord, rvnc: regenerated ventral nerve cord, obw: old body wall, rbw: regenerated body wall, d: dissepiment, omg: old midgut muscular tissue rmg: regenerated midgut muscular tissue, bv: blood vessel, arrows: mitotic cells, circles: old epithelial body layer, stars: new epithelial layer.

7.1.10. Discussion

The influence of electromagnetic waves on morphological and physiological changes of distinct cells and tissues of various species was in the focus of several experiments and based on their results Hamblin [135] concluded that probably “all life forms respond to light”. Electromagnetic waves can be ionizing and therefore harmful for cells and tissues, damaging the organisms.

In contrast, nonionizing electromagnetic waves (having small photon energy) can trigger photochemical changes within cells in which photon receptive cell organelles and molecules are located. Romanenko et al. reviewed experimental results on the effect of electromagnetic waves on biomolecules and cells and inferred that electromagnetic fields could affect the activity in cell membranes (sodium versus

potassium ion conductivities and other non-selective cation channels) [136], membrane potential, and even the cell cycle. They also suggested that THz waves do not cause tissue damage because they do not have enough energy for photoionization. Moreover, THz photon energies are in the energy range of hydrogen bonds, can cause charge transfer reactions and van der Waals interactions, meaning that even simple molecules absorb THz. However, at the same time, an *in vitro* experiment suggested that intense THz radiation causes biological hazard [55]. It was found in an *in vivo* experiment that the skin wound closure of the mice was significantly delayed by repeated femtosecond-terahertz pulse irradiation (energy up to 30 μ J, frequencies up to 2.5 THz, duration 1 hour) indicating that THz could have disadvantageous effects on biological systems [17]. The discrepancies between the published experimental results can be the consequence of the application of distinct, non-standardized biological models and various experimental protocols.

The effects of high intensity THz pulses on the standardized posterior segment regeneration of the earthworm *E. andrei*. are investigated in this study. Segment regeneration has certain discrete phases constituting the post-extirpation repairing process, like (i) sealing the slotted segment via rapid muscular contraction preventing loss of body fluids and microbial attacks, (ii) stimulation of tissue dedifferentiation and migration of mesodermal stem cells (neoblasts), scattered over all segments, to the site of the injury resulting in (iii) the formation of the regeneration blastema [137], [138]. Both dedifferentiated cells and neoblasts produce a high number of new cells by proliferation through cell division (mitosis) and their differentiation creates the new tissues and organs of the regenerating segments. In segment regeneration, there are several regulators as key players. Some of them mediate dedifferentiation, migration, and proliferation of various cells, others the differentiation of new tissues, organs, and segments, while certain regulators stop the cell division and differentiation terminating the segment formation of the abnormal cells and structures [139], [140].

No difference in the first step (wound closure) of the regeneration was found between the radiated and control animals: in all three groups, the wound was closed

at the sixth postoperative hour with the fusion of the body wall and alimentary canal tissues (Fig. 7-4). However, on the first postoperative week, more advanced development of the regeneration blastema was observed in THz-irradiated earthworms (Fig. 7-5). The regeneration blastema consists of dedifferentiated tissue cells and some migrating neoblasts [55]. Cell proliferation depends on a dynamic realignment of actin filaments in both cyto- and nucleoplasm [141]. An *in vitro* experiment showed that THz radiation modulated actin filament polymerization from soluted (globular) actin suggesting that the *in vivo* actin polymerization, mediated by any influence, contributes to the regulation of some significant processes, like gene expression, cell motility, and growth [142]. Yamazaki et al. reported that THz radiation has negligible effects on deep tissues of the human body due to strong absorption by water molecules, however, the energy of THz pulses, possibly as a shockwave, has transmitted a millimeter thick tissue in the aqueous solution and demolished actin filaments [143]. They also showed that the viability of the cell was not affected under the exposure of THz pulses.

A recent finding suggests that the blastema growth in Planarians is mediated by infrared, blue, and green light. It was found that green light exposure reduced the growth of the head blastema, while red light exposure stimulated its growth. No significant difference was found in the proliferation of neoblasts under green or red light exposure which suggests that these expositions influence the migration of the neoblasts to the amputation site [59]. In our experiments, green light did not affect segment regeneration from which we propose that in earthworms the formation of the regeneration blastema is determined by a more complex process than in Planarians and cell dedifferentiation and redifferentiation are more important in earthworm regeneration.

In our experiments, the applied THz pulses significantly stimulated the segment regeneration: irradiated animals renewed about three times higher number of segments than control specimens. The maintenance of the segments' structure and functions needs a well-controlled balance between the continuous cell proliferation

and differentiation throughout the life of an animal [144]. This balance is perturbed after any injury of the body (e.g. wound) and imbalance is a characteristic feature of the regenerating tissues. In the regenerating rat liver hepatocytes were characterized by an elevated mitotic activity but mitotic cells appeared at various points of time during the regeneration suggesting that there were unsynchronized mitotic waves during the regeneration [145]. A similar situation can appear in earthworms as well. The experimental animals could have distinct physiological states, so after the segment ablation, the cell proliferation could be started at various times. Therefore, distinct timing of the cell proliferation and differentiation could be seen in the experimental animals resulting that some specimens were characterized by intense cell proliferation while others with intense cell growing and differentiation at a fixed time of the regeneration. Nevertheless, the presented histological alterations (e.g. accumulation of mitotic cells in the epithelial layers, and extension of blood vessels) have found in THz radiated specimens which have never been seen in any animals of groups C and G.

No malformation in segment organization was found. What is more, some advantageous alterations, like more extended primordium of the VNC and more intense segment formation and advanced blood vessel development were observed (Fig. 7(c)). It is self-evident that the formation of the higher number of the renewed segments needs a lot of more new cells and their differentiation for tissue cells. New cells are produced by mitosis when semiconservative replication of the DNA and synthesis of some regulatory proteins which mediate cell divisions are carried out [142]. The effect of THz radiation on DNA molecules and cell proliferation is a debated question. In the human skin tissue model, the exposure of various cells to THz pulse at energies of 1.0 μJ and 0.1 μJ for 10 minutes resulted in DNA damage and subsequent cell growth [49]. Exposure of artificial human skin tissue to intense THz pulses caused increased expression levels of numerous genes associated with non-melanoma skin cancers, psoriasis, and atopic dermatitis. However, changes in the expression of nearly half of the epidermal differentiation complex (EDC) members were also found

suggesting that the THz-induced changes in transcription levels were opposite to disease-related changes [146].

The effect of long-term (6 hours) THz irradiation on human cells was investigated by Zhao et al. [147] It was found that long-term THz irradiation generated a specific change in gene expression resulting in abnormal chromosome number (aneuploidy) in some daughter cells. Intense exposition of cells to THz pulses induced the expression of both tumor-suppressing and oncogenic genes in human skin cells found by Hough et al. [148]. On the other hand, THz radiation at 0.38 THz and 2.52 THz did not lead to DNA damage in skin cells *in vitro*. Furthermore, no chromosomal damage was detected, and quantified cell proliferation was found to be unaffected by the exposure [51]. A recent study suggests that THz wave exposure with very low intensity does not affect cell proliferation or cell growth rates [13].

At present, there is only weak evidence that THz pulses can influence cell proliferation (mitosis) and differentiation. Bock et al. investigated the effect of broadband THz radiation on mammalian (mouse) stem cells. They found that radiation-induced specific changes in cellular functions were closely related to DNA-directed gene transcription. Surveying of gene expression, they found that 11% of genes responded to the applied THz radiation, either upregulated or downregulated, and based on the accelerated cell differentiation they concluded that THz radiation could be a potential tool for cellular reprogramming [15]. The segment regeneration needs both intense cell proliferation and differentiation. However, details of the regulation are not known yet. We found that the applied THz pulses stimulated the formation of a high number of new segments. Based on this, we suppose that THz pulses influence the activity of various biomolecules like proteins, DNA, and RNA due to the conformational changes as was reported by Lee [46].

Investigating the effect of THz pulses on human induced pluripotent stem cells THz pulses could alter the expression of certain genes and they were driven by zinc–finger transcription factors and it was supposed that the local intracellular concentration of metal ions, such as Zn^{2+} , was changed by the effective electrical force of the applied

THz pulse. However, there is a large phylogenetic distance between humans and earthworms, the zinc-finger transcription factors are probably present in the latter one as well, as it has been found by Tachizaki et al. [149]. A putative zinc-finger protein as a gene activator was identified in a lumbricid earthworm [150], therefore there is a possibility that similar molecular and cellular processes are stimulated by THz pulses in earthworms similarly to human cells.

Currently, segment regeneration is a largely unknown process characterized by some enigmatic cytological and histological alterations. However, there is some experimental evidence that anatomical, physiological, and cellular factors influence the kinetics of segment regeneration. The best documented neural dependence of regeneration was promulgated by Morgan [24] for the first time and supported by some experimental evidences later. The formation of the regeneration blastema is started at the cut end of the VNC from which neural processes outgrow and spread amongst tissue cells [79]. Discharged neural substances, certain neurotransmitters, and neurohormones stimulate the segment regeneration by regulating the functioning of various tissues [19], [20]. Tan et al. found that the primary cultured neurons responded to the THz radiation and the induced biological effects were positively correlated with the exposure time of the THz waves [14]. The marked decrease in the neurotransmitter content (glutamate) of some neurons were detected as well. An *in vivo* THz radiation can generate a similar neurotransmitter release from neurons stimulating the formation of the regeneration blastema and differentiation of its cells. Although, Borovkova et al. showed a dose-dependent cytotoxic effect of THz radiation on glial cells [55], in our experiments no significant number of necrotic or apoptotic cells was found in any tissues. In contrast to the effect of repeated femtosecond-THz radiation (energy up to 30 μ J, frequencies up to 2.5 THz, duration 1 hour) applied in a wound-healing experiment [17], the used THz exposure (energy 5 μ J, 0.3 THz frequency, irradiation time 5 min) in our experiments has an advantageous effect on wound healing and it has been experimentally proven on tissue and organ regeneration of earthworms. This strongly suggests that the parameters of THz

exposure (energy, frequency, irradiation time) can significantly influence its biological effects.

Segment regeneration of earthworms can be a useful model to investigate the effect of various factors on the phenotypic changes (both anatomical and physiological) at the organism level. Certain physical effects, like temperature, modify the kinetics of segment regeneration e.g. the long-term (several days) cooling of the experimental animals after the surgical intervention resulted in lower segment regeneration in various earthworm species [151]. Moment investigated the effect of the ionizing X-ray irradiation on the five posteriormost segments located afore the transection and found that its effect on the regeneration was dose-dependent. Only a high dose of X-ray radiation (from 20,000 R) blocked the formation of new tissues and organs [152]. Based on the observations mentioned above, we suppose that the kinetics of segment formation is an effective indicator of both inhibitory and stimulatory effects of various factors. Therefore, it can be used as a model at the organism level to investigate the biological effects of distinct electromagnetic waves.

7.1.11. Conclusion

The presented results show that the posterior segment regeneration of earthworms is a suitable model to investigate the biological effects of THz pulses at the organism level and suggest that there are certain interactions between THz radiation and biomolecules (proteins, nucleic acids, etc.), cells, and tissues. The applied intense THz pulses significantly stimulated the segment regeneration. No abnormal tissue or segment development occurred in the experimental animals during the four-week-long experiments. Based on these findings, we can propose that the applied THz radiation has beneficial effects on both cell proliferation and differentiation, and on tissue development. Further *in vivo* experiments are needed to ascertain the exact influence of THz radiation on cell proliferation and differentiation. The present study can contribute to the improvement of biomedical application of THz pulses.

7.2. Absorption of pulsed terahertz and optical radiation in earthworm tissue and its heating effect

7.2.1 Optical and THz transmission measurements

The experimental setup is shown in Fig 7-8. The different sample positions allowed to switch quickly between the three types of irradiation pulses. The infrared (IR) laser pulses of 1030 nm central wavelength, 180 fs pulse duration, up to 1 mJ pulse energy, and controlled intensity were delivered to position IR (Fig. 7-8) by an Yb:KGW regenerative amplifier operating at 1 kHz repetition rate. Before the sample, an iris diaphragm reduced the beam size to about 2 mm, a diameter smaller than the sample size. Green laser pulses of 515 nm wavelength were produced by phase-matched second-harmonic generation of the infrared laser pulses in a BBO crystal. Reflection on a dichroic mirror was used to separate the green light from the infrared fundamental and to direct it to position G (Fig. 7-8) through another 2-mm iris aperture. The infrared and green laser powers, transmitted through the sample and the sample holder glass plate, were measured by a laser power meter (Gentec, model XLP12-3S-H2-D0). To obtain transmission values, reference measurements with the sample holder plate were carried out.

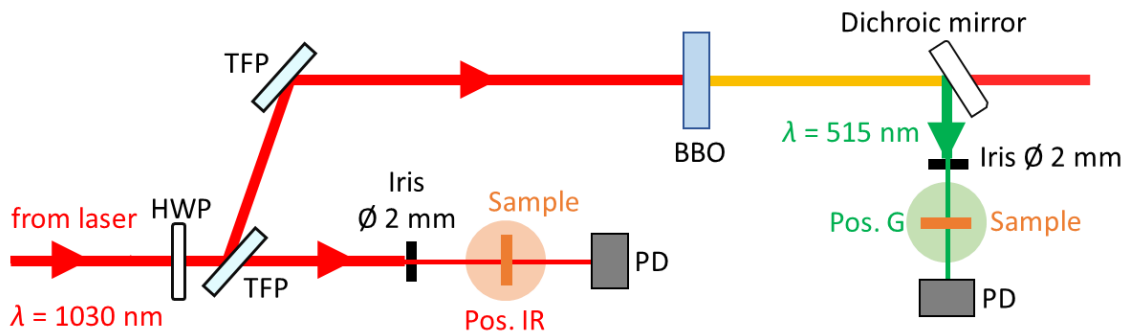


Figure 7-8. Optical layout of the two-color optical irradiation setup. HWP: half-wave retardation plate, TFP: thin-film polarizer, PD: photodiode.

THz transmission measurements were carried out in a commercial time-domain THz spectrometer (TDS) of model Tera K8 manufactured by Menlo Systems. Nearly-single-cycle THz pulses were generated in the TDS with a biased photoconductive

antenna illuminated by femtosecond laser pulses. The TDS configuration was similar to that shown in [153]. In our case, the THz pulses were collimated and focused onto the sample by a pair of TPX polymethylpentene lenses. Another pair of TPX lenses was relay imaging the sample position onto the detector photoconductive antenna. The peak of the amplitude spectrum of the broadband THz pulses was at about 0.65 THz. For the investigated strongly absorbing tissue samples, the useful spectral range was extending from about 0.2 THz to 2.0 THz. The THz pulses transmitted through the sample and the holder assembly (in reference measurements only through the holder assembly), were collimated and focused by another pair of TPX lenses onto a second, unbiased photoconductive antenna for waveform measurement. For this purpose, synchronized femtosecond laser pulses were overlapped with a variable delay with the THz pulses on the photoconductive antenna.

7.2.2 Tissue samples

Tissue samples were surgically isolated from earthworms *Eisenia Andrei*. The selected specimens were kept on wetted paper wadding for three days to remove gut content. The samples were isolated from the middle part of the earthworm body (Fig. 7-9a). For the optical transmission measurements, animals of different size were selected in order to provide dorsal body wall tissue samples of different thicknesses ($d_{BW} = 0.17$ mm, 0.23 mm, and 0.33 mm) but with the same structure (Fig. 7-9b). Pieces of the body wall of about 2.5 mm × 10 mm area were surgically isolated. The body wall contained the epithelial layer and the circular and longitudinal muscular layers. In addition, a sample containing the whole-body cross-section was also used with a thickness of 1.5 mm. After surgical isolation, the tissues samples were placed on 0.18 mm thick glass plates (microscope cover plates, Fig. 7-9.c) and covered by thin plastic tapes to prevent fast drying out. The plastic covering tape was removed during the radiation transmission measurements. The thickness was measured on small pieces cut off from the sample by using an optical microscope with a scale. Optical transmission measurements were carried out one hour after sample preparation.

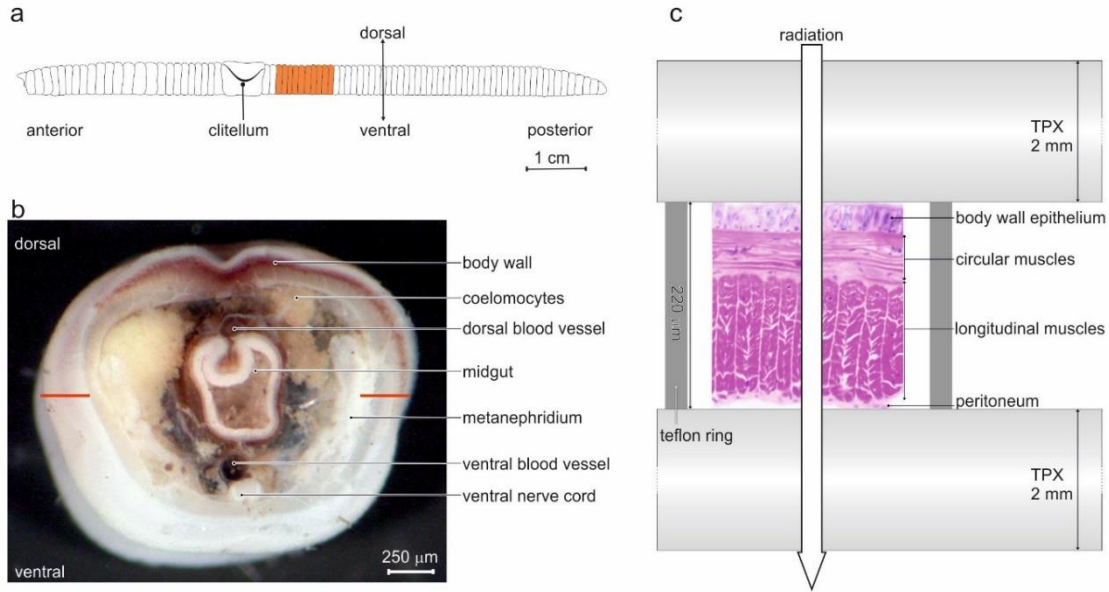


Figure 7-9. (a) Schematic drawing of the earthworm *Eisenia andrei*. The colouring shows the part of the body from which the irradiated samples were prepared. (b) Photograph of the body cross-section of the earthworm. The red lines indicate the surgical cuts for tissue sample preparation. (c) Photo of a sample mounted for optical transmission measurement. Schematic drawing of sample irradiation with a body wall tissue of thickness is d_{BW} (not to scale).

For the THz transmission measurements, dorsal body wall tissue samples of 0.22 mm and 0.33 mm thicknesses were used. Due to low transmission, results are shown here only for the thinner sample. After surgical isolation, the tissues samples were placed on 2 mm thickness of TPX plates (Fig. 7-9.c) and covered by another identical plate to prevent fast drying out. The sample thickness was precisely fixed by a Teflon spacer between the PMP plates.

7.2.3 Experimental results

The power transmission $T(d)$ through a sample of thickness d was determined from measurements of the incoming and transmitted power according to the following approximate relation:

$$T(d) = \frac{P(d)}{T_g \cdot P_0} \quad (14)$$

Here, P_0 is the incident power, $P(d)$ is the transmitted power through a sample of thickness d placed on the glass substrate with transmission T_g . The substrate

transmission could not be measured directly when the sample was attached to it. Therefore, it was estimated from a reference measurement of the substrate in air, thus including reflection losses from two air-glass surfaces and the absorption losses in the bulk of the glass material. Consequently, $T(d)$ includes the absorption losses within the tissue and the (reflection and scattering) losses at the input air-tissue boundary surface (see also Equation (15) below).

Figure.7-10 shows, on a logarithmic scale, the measured power transmission for the green and IR laser pulses of 515 nm and 1030 nm central wavelengths, respectively, as functions of the sample tissue thickness. The measurements were carried out about one hour after surgical isolation of the tissues from the earthworms. At the shorter wavelength of 515 nm, the attenuation is relatively strong and uniform. The transmitted power shows a simple exponential dependence on the tissue thickness to a reasonably good approximation (Fig. 7-10a). This indicates similar absorption properties for the body wall (0.17 – 0.33 mm thickness) and the inner part of the body (1.5 mm). About 66% of the radiation is transmitted through a 0.33 mm thick body wall, and only about 22% of the incoming power is transmitted through the 1.5 mm thick sample containing the whole body cross section.

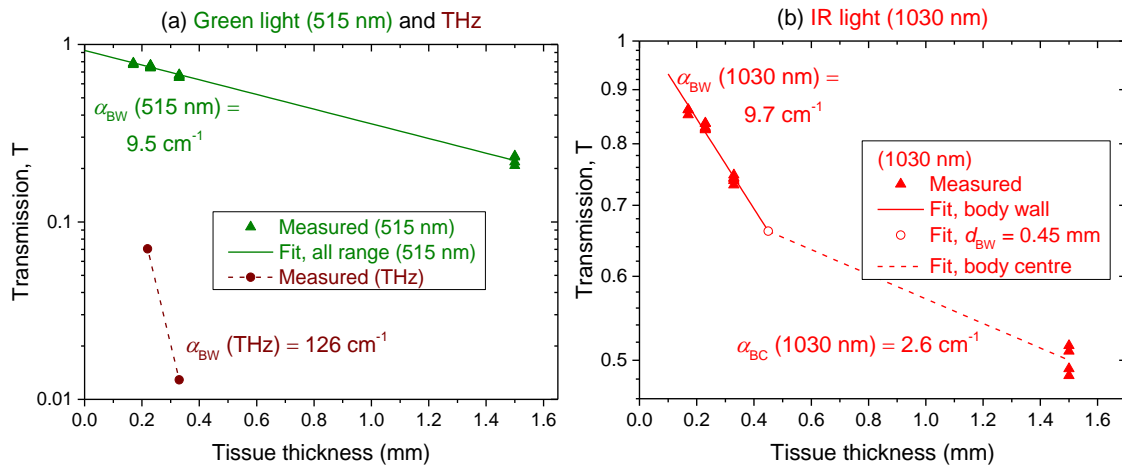


Figure 7-10. (a) Measured power transmission for green light and THz radiation as function of the sample tissue thickness. (b) Measured power transmission for infrared light as function of the sample tissue thickness. The lines corresponding to green and infrared indicate exponential fit curves. The dashed line in case of the THz data is a guide to the eye. The empty symbol in (b) indicates the body-wall fit extrapolated to 0.45 mm thickness.

The dependence on the sample thickness of the transmitted IR power through the body wall (up to 0.33 mm thickness) is similar to the case of the green light (Fig 7-10b). About 74% of the incoming IR radiation is transmitted through 0.33 mm of body wall. However, the IR transmission through the body centre is significantly larger than for green. About 50% of the IR radiation is transmitted through a 1.5 mm thick sample with the full body cross-section. Thus, there is a noticeable difference between the transmission of the body wall and that of the body centre, in contrast to green light.

Figure 7-11a shows the time dependence of the electric field strength of the transmitted THz pulses as function of time, measured by TDS. The body-wall tissue sample had a thickness of 0.22 mm (red curve). The reference pulse was passing through the empty sample holder assembly (black curve). We note that over a time interval of 2 hours, less than 3% relative change in the THz transmission was observed, thus covering the sample efficiently prevented it from drying out. The measurement was carried out about one hour after surgical isolation of the samples. The electric fields, shown in arbitrary units, are multiplied by different constant values for better comparability. The frequency-dependent intensity absorption coefficient of the body wall, calculated

from the measured THz waveforms after Fourier transformation, is shown in (Fig. 7-11.b) as function of the THz frequency.

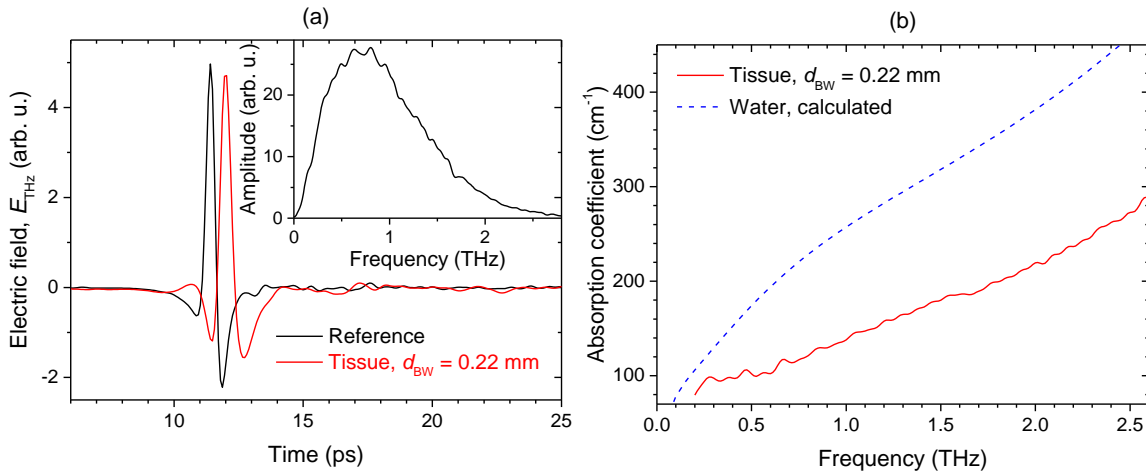


Figure 7-11. (a) Electric field strength of the transmitted THz pulses as function of time, measured by TDS. The body-wall tissue sample had a thickness of 0.22 mm (red curve). The reference pulse was passing through the empty sample holder assembly (black curve). The inset shows the amplitude spectrum of the transmitted reference pulse. (b) Intensity absorption coefficient of the body wall as function of the THz frequency, calculated from the measured THz waveforms. The calculated absorption coefficient of water [46], [154] is shown for comparison.

It is possible to calculate the spectrally integrated power transmission for the THz pulses from the TDS measurements. Figure 7-11a includes such THz power transmission values for two different body-wall tissue thicknesses of 0.22 mm and 0.33 mm. The transmission was calculated by taking the ratio of the relative power of THz pulses with and without sample. Relative power values were obtained by integrating the power spectra from the TDS measurements from 0.15 THz to 2.5 THz. The THz power transmission, calculated in this way, gives a body-wall absorption coefficient of 126 cm^{-1} (Fig 7-10a). This coincides well with the average absorption coefficient in the range of about 0.5 THz to 1 THz (Fig 7-11b). The reason of this coincidence is the spectral amplitude maximum in this range (see inset in Fig 7-11a).

7.2.4 Discussion

7.2.4.1 Tissue absorption coefficients

The purpose of the transmission measurements was to obtain values for α_{BW} and α_{BC} , the (average) absorption coefficients of the earthworm body wall and body centre, respectively. The measured dependence of the power transmission T (defined in Equation 14) on the sample thickness and structure was approximated by the fit function

$$T(d = d_{BW} + d_{BC}) = \tau \cdot e^{-\alpha_{BW} \cdot d_{BW}} \cdot e^{-\alpha_{BC} \cdot d_{BC}}. \quad (15)$$

Here, d , d_{BW} , and d_{BC} are the thicknesses of the full sample, the body wall, and the body centre, respectively. The thinner samples (up to 0.33 mm thickness) were composed of body wall tissue only, therefore $d = d_{BW}$ holds in these cases. For the sample containing the full body cross-section, the full thickness was $d = d_{BW} + d_{BC} = 1.5$ mm, with $d_{BW} = 0.45$ mm and $d_{BC} = 1.05$ mm. Note that in this case, d_{BW} refers to the total thickness of the dorsal and the ventral body walls. In Equation (15), τ denotes the losses at the input air-tissue boundary surface, as already mentioned in connection to Equation 14.

The infrared absorption coefficients were obtained by the following fitting procedure. First, the model function given by Equation (15) was used with $d_{BC} = 0$ to determine α_{BW} from the measurements with the thinner samples composed of body wall only. Then a second fit was carried out with $d_{BW} = 0.45$ mm and $d_{BC} = 1.05$ mm, with α_{BC} as the only free parameter. In this case, only the measured data for the sample with full body cross-section were considered.

The results of the curve fitting, together with the obtained absorption coefficient values, are shown in (Figure 7-10a) for green light, in (Figure 7-10b) for IR light. Numerical values of the tissue absorption coefficients for all three radiation types are summarized in Table 7-1. As mentioned earlier, all absorption coefficients correspond to measurements carried out one hour after surgical removal of the tissue samples from the animals.

Table 7-1. Measured absorption coefficients of the *Eisenia andrei* body-wall tissue samples for green and infrared light, and for a few selected THz frequencies. For THz radiation, average values for two frequency intervals are also given, which are considered in the discussion.

Wavelength, λ [nm] or frequency, ν [THz]	Absorption coefficient, α_{BW} [cm^{-1}]
515 nm	10.6
1030 nm	9.8
0.2 THz	80
0.3 THz	97
0.5 THz	102
1.0 THz	138
1.5 THz	180
2.0 THz	220
2.5 THz	273
0.2 THz – 0.5 THz	97 (average, used in heat calculation)
0.15 THz – 2.5 THz	126 (average, Fig 7-10a)

For green light of 515 nm wavelength, the fitting procedure as described above delivers nearly equal absorption coefficients for the body wall and the body centre ($\alpha_{BW} = 10.6 \text{ cm}^{-1}$ and $\alpha_{BC} = 9.2 \text{ cm}^{-1}$, respectively; not shown in (Figure 7-10a). Hence, a good agreement for all sample thicknesses can be obtained by using a simplified fit function with identical values for both absorption coefficients (Figure 7-10a). This delivers the value $\alpha_{BW} = \alpha_{BC} = 9.5 \text{ cm}^{-1}$.

For IR light of 1030 nm wavelength, it is necessary to use different absorption coefficients for the body wall and the body centre (Figure 7-10b). The fitting procedure delivers $\alpha_{BW} = 9.8 \text{ cm}^{-1}$ (Table 7-1) and $\alpha_{BC} = 2.7 \text{ cm}^{-1}$, respectively. The body-wall absorption coefficient is very similar to that for the green light, but for the body centre it is about 3.5 times smaller. We note that a moderate increase of the IR body-wall absorption coefficient with increasing thickness can be observed (Figure 7-10b).

In the THz range, the frequency-dependent absorption coefficient of the body wall was determined from the TDS measurements. First, the amplitude spectra $E_s(\omega)$

and $E_r(\omega)$ s sample and r reference were calculated by Fourier transformation from the measured temporal waveforms with the tissue sample and the reference without the sample, respectively. The absorption coefficient was calculated from the following formula [153]:

$$\alpha_{BW}(\omega) = -\frac{2}{d_{BW}} \ln \left[\frac{|E_s(\omega)|}{|E_r(\omega)|} \right]. \quad (16)$$

Concerning the interfaces and surfaces, the difference between the reference and the sample measurements only is that the two inner interfaces are TPX-air (and air-TPX) for the reference measurement, whereas they are TPX-tissue (and tissue-TPX) for sample the measurement. Near 0.2 THz, above which our TDS measurements are considered to be reliable, the tissue refractive index is estimated to be smaller than 2.5 and it is rapidly decreasing to values near 2 with increasing frequency (see Ref. [155] for comparison with other tissue types). Since the ratios of the refractive indices of the materials on the two sides of the interfaces are about the reciprocals of each other, the caused Fresnel losses are about the same. More precisely, with the refractive indices $n_{TPX} = 1.46$ for TPX, $n_{air} = 1$ for air, and $n_{BW} = 2$ (2.5) for the body-wall tissue, we obtain a relative error in the calculated tissue absorption coefficient of less than 1% (3%) for the investigated sample thicknesses. This is smaller than the estimated uncertainty of 10% to 15% originating from sample-by-sample variation and the limited thickness measurement accuracy.

The obtained intensity absorption coefficient for the body wall is plotted in (Fig 7-11b) as function of the THz frequency. It steadily increases from about 80 cm^{-1} at 0.2 THz to about 220 cm^{-1} at 2.0 THz. For comparison, the absorption coefficient of pure water increases from about 106 cm^{-1} at 0.2 THz to about 382 cm^{-1} at 2.0 THz [46], [154]. The absorption coefficient of pure water, calculated from a room-temperature dispersion formula [46], [154], also can be seen in (Figure 7-11b). Thus, the absorption coefficient of the tissue samples measured here is about 60% to 75% of that of pure water. The water content of *Eisenia Andrei* specimens was measured to be 81.5%

(82.7%) in the anterior (postclitellar) part of the body. The measured tissue and water absorption coefficients are given for a few selected THz frequencies in Table 7-1.

7.2.4.2 Estimation of the heating effect

The simplest direct effect of radiation on a tissue can be heating due to the absorbed power. A steady-state heat equation was used to model the heating effect of radiation on the tissue and to compare it to pure water. The beam was assumed to propagate into the z direction. For the sake of simplicity, temperature variation only in z direction was considered. Such an approximation is suitable for the body wall tissue, where the thickness of the tissue (0.22 mm in this case) is significantly smaller than its lateral size (≥ 2.5 mm) and the typical size of a focused THz beam (≥ 2 mm for frequencies of 0.2–0.5 THz). Furthermore, a homogeneous medium was assumed with the absorption coefficient $\alpha_{BW} = 97 \text{ cm}^{-1}$. This corresponds to the average measured absorption coefficient of the body wall tissue in the 0.2 THz to 0.5 THz range. This choice is justified by the spectral band of the most intense part of the THz pulses used in our results [16]. The following one-dimensional heat equation was solved (see for example [156]–[158]):

$$\Delta T(z) = \frac{\partial^2}{\partial z^2} T(z) = -\frac{1}{k} q(z). \quad (17)$$

$$q(z) = \alpha_{BW} I_0 e^{-\alpha_{BW} z} \quad (18)$$

Here, $T(z)$ is the steady-state temperature at tissue depth z . The thermal conductivity k was assumed to be constant, i.e. independent of temperature and position. Temperature independence is justified by the small increases in temperature, as discussed below.

For the thermal conductivity of the body-wall tissue sample, an estimated value of $k = 0.50 \text{ W m}^{-1} \text{ K}^{-1}$ was used here. For comparison, the room-temperature (at 293 K) thermal conductivity of water is $0.60 \text{ W m}^{-1} \text{ K}^{-1}$ [159]. We note that thermal conductivity values reported in the literature for biological tissues vary in a broad range. The values depend on species, tissue type, *in vivo* or *in vitro* conditions,

temperature [157], hydration level, and other circumstances. For example, for *in vivo* conditions, blood circulation can have a substantial effect [160]. Typical reported *in vivo* values for animal skin or muscle tissues are in the range 0.5–0.6 W m⁻¹ K⁻¹ [158]–[161].

In case of heating caused by radiation absorption, the dissipated power density in unit W m⁻³ is given by Equation (18), where I_0 (of unit W m⁻²) is the average intensity at $z = 0$. The boundary conditions were defined as follows:

$$\left. \frac{\partial T(z)}{\partial z} \right|_{z=0} = 0, \quad (19)$$

$$T(d_{BW}) = T_a. \quad (20)$$

It was assumed that there is no heat loss to air or other surrounding medium at the entrance side of the sample ($z = 0$), which is expressed by Equation (19). At the back side of the sample, the glass substrate was considered to act as a heat sink at the constant ambient temperature T_a , as described by Equation (20). Because this assumption overestimates the effect of the glass substrate and other effects, such as heat loss by air convection, are neglected, the temperature values given below can be regarded as an estimation of the order of magnitude for the heating effect of THz radiation. The solution of the heat Equation (17), obeying such boundary conditions, can be given as:

$$T(z) = T_a + \frac{I_0}{k} (d_{BW} - z) + \frac{I_0}{\alpha_{BW} k} (e^{-\alpha_{BW} d_{BW}} - e^{-\alpha_{BW} z}). \quad (21)$$

The calculated results for the THz intensity and the temperature increase are shown in (Figure 7-12) for the case of THz radiation propagating through 0.22 mm thickness of body wall. The incident average intensity inside the tissue was assumed to be about 160 mW cm⁻². This corresponds to the situation used in our previous work [16] with 5 μJ pulse energy, 1 kHz repetition rate, and 1 mm focused THz beam radius, giving 5 mW average input power. About 12% of THz radiation is transmitted through the sample (Figure 7-12a). The largest increase in sample temperature of 0.41 K is

obtained at the input surface $z = 0$ (Figure 7-12b). Such a small temperature increase suggests that heating may have negligible effect on biological functions. Comparison with pure water (with an average absorption coefficient of 141 cm^{-1} in the 0.2 THz to 0.5 THz range) shows very similar temperature increase, due to the similar absorption coefficient of water. For comparison, Fig.7-12 also shows the intensity and temperature increase as functions of the penetration depth for the green and IR optical radiations. These data were calculated with the measured body-wall absorption coefficients as given in the first two rows of Table 7-1, whereby the same 160 mW cm^{-2} average input intensity was assumed as in case of the THz radiation. For optical radiation, the penetration depth is much larger (about 1 mm) and the temperature increase is even smaller (less than 0.1 K).

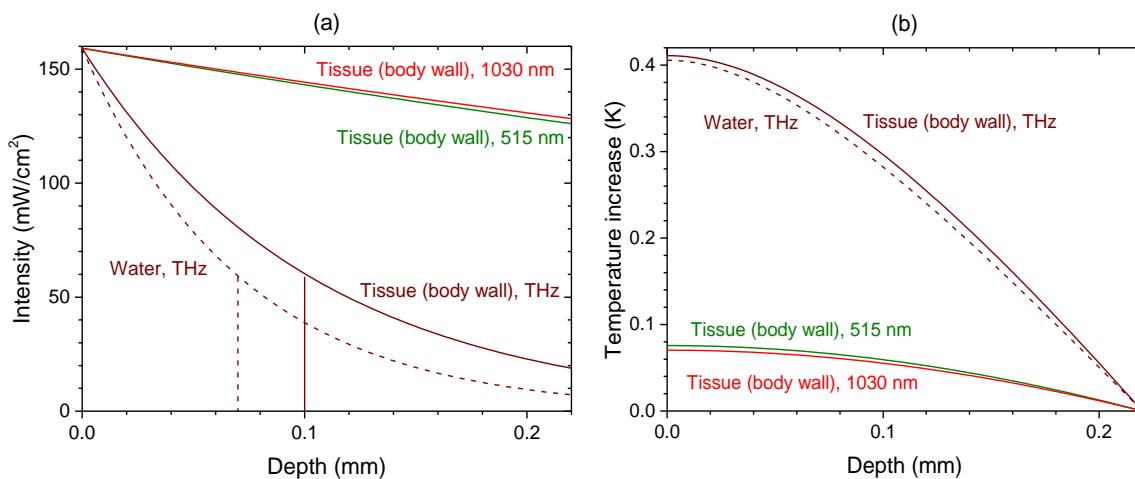


Figure 7-12. Calculated intensity (a) and temperature increase (b) in body wall tissue caused by irradiation with THz, green, and IR pulses. The dashed lines show the calculation for pure water and THz radiation. Both for the tissue and water, THz average absorption coefficients ($\bar{\alpha}$) for the 0.2 THz to 0.5 THz range were used. The vertical lines show the THz penetration depths ($1/\bar{\alpha}$) in tissue (solid line) and water (dashed line).

Based on the small (about 0.4 K) estimated temperature elevation, the observed very pronounced stimulation of segment regeneration by THz irradiation [16] could be dominated by effects other than heating. For complex biological materials, it is very challenging to reveal the details of the various mechanisms of THz radiation because of the wealth of degrees of freedom for interaction. However, the temperature increase

is proportional to the incident power or intensity according to Equations (17) and (21). Because of this, current cutting-edge high-intensity THz sources with mJ-level pulse energies (see e.g. [162]) can have very significant direct heating effects of tens-of-K, especially for high repetition rates and/or long exposure times.

7.2.5. Conclusion

Transmission of green (515 nm), near-infrared (1030 nm), and THz pulses through biological tissue was studied. As model, tissue samples taken from *Eisenia andrei* earthworms of different sizes were used, containing the epithelial layer and the circular and longitudinal muscles. Also samples of larger thickness, containing the complete cross-section of the animal, were investigated for comparison. Whereas the transmitted power for the green optical pulses reasonably followed the Beer-Lambert law of exponential attenuation for all thicknesses and tissue structures, near-infrared pulses were significantly deviating from this, which hints to the dependence on tissue structure. The tissue absorption coefficient was measured by time-domain THz spectroscopy in the frequency range from 0.2 THz to 2.5 THz. The absorption varies from 80 cm^{-1} at 0.2 THz to 273 cm^{-1} at 2.5 THz. Simple model calculations indicate that THz pulses of $5 \mu\text{J}$ energy and 1 kHz repetition rate (5 mW average power), as used in our study [16], cause a small temperature increase of about 0.41 K, suggesting that heating may be less important for biological effects. This can be drastically different for mJ-level THz pulse energies, which have become available recently.

The knowledge of tissue absorption properties is an important prerequisite to estimate the biological effectiveness of radiation. It can also set the framework to investigate in detail the mechanisms of various biological effects. Intense pulsed THz radiation can have a profound biological impact. Despite small penetration depths of about 0.1 mm for the 0.2 THz to 2.5 THz range considered in the present work, global (nonthermal) biological effects can occur. In this context, it is also of interest to extend the absorption measurements to still lower frequencies, where the penetration depth

can be larger. It can be anticipated that global, organism-level effects can occur in other types of living creatures, even in case of larger-size organisms.

8. Thesis statements

The experimental study presented in this work clearly demonstrated that intense THz pulses can have a very strong, global effect on living organisms. This is a highly nontrivial statement, given the shallow penetration depth of THz radiation into living biological tissues with large water content. The topic of high-level biological effects of THz radiation is a new one. Despite the availability of efficient and intense table-top pulsed THz sources since two decades, still no detailed and coherent knowledge exists on their biological effectiveness and the interaction pathways. This lack of knowledge motivated me to investigate the effects of THz pulses on a specific animal model, the *Eisenia andrei* earthworm, at the cell, tissue, and organism level. The findings from my efforts can be summarized in the following thesis statements.

1- THz irradiation of excised *Eisenia andrei* earthworms was shown to cause overriding of the genetically determined, endogenously mediated segment renewing capacity of the model animal. Single-cycle THz pulses of 5 μJ energy, 0.30 THz mean frequency, 293 kV/cm peak electric field, and 1 kHz repetition rate stimulated the cell proliferation (indicated by the high number of mitotic cells) and both histogenesis and organogenesis, producing a significantly higher number of regenerated segments. The most conspicuous alteration in THz-treated animals was the more intense development of the new central nervous system and blood vessels. These results clearly demonstrate that THz pulses are capable to efficiently trigger biological processes and suggest potential applications in medicine.

2- The transmission of THz, near-infrared (1030 nm), and green (515 nm) pulses through *Eisenia andrei* body wall is studied, which consists of epithelial layer and circular and longitudinal muscles. Samples with the full-body cross-section were also investigated. The transmitted power for the green pulses followed the Beer-Lambert law of exponential attenuation for all thicknesses and tissue structures. Different body wall and body center absorption coefficients were found in case of infrared pulses. In

the THz range, the body wall absorption coefficient steadily increases from about 80 cm^{-1} at 0.2 THz to about 273 cm^{-1} at 2.5 THz.

3- Numerical estimation indicated that THz pulses of 5 μJ energy and 1 kHz repetition rate (5 mW average power) cause only a small temperature increase of about 0.4 K, suggesting that heating has a minor contribution to biological effectiveness.

9. Tézispontok

Az ebben a munkában bemutatott kísérleti tanulmány egyértelműen bebizonyította, hogy az intenzív THz-es impulzusok nagyon erős, globális hatást gyakorolhatnak az élő szervezetekre. Ez egy nagyon nem triviális kijelentés, tekintve, hogy a THz-es sugárzás kismértékben behatol a nagy víztartalmú élő biológiai szövetekbe. Új téma a THz-es sugárzás magas szintű biológiai hatásainak témaköre. Annak ellenére, hogy két évtizede rendelkezésre állnak hatékony és intenzív asztali pulzáló THz-es források, még mindig nem áll rendelkezésre részletes és koherens tudás a biológiai hatékonyságukról és a kölcsönhatási útvonalokról. Ez az ismeretek hiánya késztetett arra, hogy megvizsgáljam a THz-es impulzusok hatását egy adott állatmodellre, az *Eisenia andrei* gilisztára, sejt-, szövet- és szervezeti szinten. Erőfeszítéseim eredményeit a következő tézisállításokban foglalhatjuk össze.

1- A kimetszett *Eisenia andrei* giliszták THz-es besugárzása a modellállat genetikailag meghatározott, endogén közvetített szegmensmegújító képességét felülírja. Az 5 μ energiájú, 0.30 THz-es átlagos frekvenciájú, 293 kV/cm-es csúcs elektromos térerősségű, 1 kHz-es ismétlési sebességű egyciklusú THz-es impulzusok stimulálták a sejtproliferációt (amit a mitotikus sejtek nagy száma jelez), valamint a hisztogenezist és az organogenezist is, ami lényegesen nagyobb számú regenerált szegmens. A THz-vel kezelt állatokban a legszembetűnőbb változás az új központi idegrendszer és az erek intenzívebb fejlődése volt. Ezek az eredmények egyértelműen bizonyítják, hogy a THz-es impulzusok képesek hatékonyan elindítani a biológiai folyamatokat, és potenciális gyógyászati alkalmazásokat javasolnak.

2- A THz-es, közeli infravörös (1030 nm) és zöld (515 nm) impulzusok átvitelét vizsgáljuk az *Eisenia andrei* testfalán, amely hámrétegből, valamint körkörös és hosszanti izomzatból áll. A teljes test keresztmetszetű mintákat is megvizsgáltuk. A zöld impulzusok átvitt teljesítménye követte az exponenciális csillapítás Beer-Lambert törvényét minden vastagság és szövetszerkezet esetén. Az infravörös impulzusok esetében eltérő testfal és testközép abszorpciók együtthatókat találtunk. A THz-es

tartományban a testfal abszorpciós együtthatója folyamatosan növekszik körülbelül 80 cm^{-1} -ről $0,2 \text{ THz}$ -en körülbelül 273 cm^{-1} re 2.5 THz -en.

3- A numerikus becslések azt mutatták, hogy az $5 \mu\text{J}$ energiájú és 1 kHz -es ismétlési frekvenciájú THz -es impulzusok (5 mW átlagteljesítmény) csak kismértékű, körülbelül 0.4 K hőmérsékletnövekedést okoznak, ami arra utal, hogy a fűtés kis mértékben járul hozzá a biológiai hatékonysághoz.

10. Publication list

1. Publications in the topic of thesis

- **M. Abufadda *et al.***, “Terahertz pulses induce segment renewal via cell proliferation and differentiation overriding the endogenous regeneration program of the earthworm *Eisenia andrei*,” *Biomed. Opt. Express*, vol. 12, no. 4, pp. 1947–1961, 2021, doi: 10.1364/boe.416158 [16].
- **M. H. Abufadda *et al.***, “Absorption of Pulsed Terahertz and Optical Radiation in Earthworm Tissue and its Heating Effect,” *J. Infrared, Millimeter, Terahertz Waves*, 2021[163].

2. Non-refereed conference abstracts in the topic of thesis

- **M. Abufadda**, P. Nugraha, S. Li, J. Hebling, J. A. Fülöp, and L. Molnár, “Effects of THz pulses on the regeneration of the earthworm *Eisenia Andria*,” *Conf. Terahertz Sci. Technol. (TST), Berlin, Ger.*, 2018.
- **M. Abufadda**, A. Erdélyi, G. Krizsán, J. Hebling, J. A. Fülöp, and L. Molnár, “THz pulses stimulate the tail segment regeneration of the earthworm *Eisenia Andrei*,” *Opt. InfoBase Conf. Pap.*, vol. Part F140-CLEO_Europe 2019, no. 137, p. **7281**, 2019.

11. Acknowledgment

I have completed the Doctoral School and wrote this dissertation at the Institute of Physics, Faculty of Science, University of Pécs (Hungary). Research for this thesis was performed at the High-Field THz lab at Szentágotthai research centre and developmental biology lab at the University of Pécs (Hungary) during my Ph.D. in Physics program. My personal activity on the topic of this dissertation is primarily based on experimental lab-work and data evaluation. However theoretical simulations and calculations are an integral part of this scientific work.

I am thankful to both of my supervisors Prof. József Fülöp and Prof. László Molnár, their doors have always been open to my research questions and problems. I would also like to thank them for investing efforts in supervision my research and spending time reading the manuscripts and thesis. A special thanks also to the mind, motor, and head of the doctoral school in the physics department Prof. Janos Hebling for all his experience supports. Which gave us confidence every time. I would thank all my colleagues in the physics department, and other colleagues in the biology department, who helped me during my Ph.D. study. Finally, I would present this thesis first of all to my ambition, and trust of my God, science, and to my mother sharing with my brother Ali Abufadda they were very careful to success on my study.

12. References

- [1] C. Fattering and D. Grischkowsky, "Point source terahertz optics," *Applied Physics Letters*, vol. 53, no. 16. pp. 1480–1482, 1988, doi: 10.1063/1.99971.
- [2] W. Ghann and J. Uddin, "Terahertz Spectroscopy - A Cutting Edge Technology," *Terahertz Spectrosc. - A Cut. Edge Technol.*, pp. 3–20, 2017, doi: 10.5772/62805.
- [3] <https://physicsinventions.com/>, "terasense-develops-promising-terahertz-and-sub-thz-frequency-range-innovative-imaging-equipment-2/," 2015.
- [4] R. H. W. Funk, T. Monsees, and N. Özkucur, "Electromagnetic effects - From cell biology to medicine," *Prog. Histochem. Cytochem.*, vol. 43, no. 4, pp. 177–264, 2009, doi: 10.1016/j.proghi.2008.07.001.
- [5] E. Bachanek, T., SAPUŁA, M., JARMOLIŃSKA, K. and WOLAŃSKA, "Effect of electromagnetic field on tissues of the oral cavity of rats. A preliminary study.," *Bull Vet Inst Pulawy*, vol. 54, pp. 683–685, 2010.
- [6] S. E. Abo-Neima, H. A. Motaweh, and M. F. Ragab, "Effects of Electric Field on Histopathological Study, Electrical Properties and Enzymes Function of Liver of Albino Rats," *J. Adv. Phys.*, vol. 4, no. 2, pp. 120–128, 2015, doi: 10.1166/jap.2015.1179.
- [7] S. Ebrahim, A. E. Azab, M. O. Albasha, and N. Albishti, "THE BIOLOGICAL EFFECTS OF ELECTROMAGNETIC FIELDS ON HUMAN AND EXPERIMENTAL ANIMALS Chronic kidney diseases View project," no. October, pp. 105–121, 2016.
- [8] L. Zhao, Y.-H. Hao, and R.-Y. Peng, "Advances in the biological effects of terahertz wave radiation," *Mil. Med. Res.*, vol. 1, no. 1, pp. 1–4, 2014, doi: 10.1186/s40779-014-0026-x.
- [9] G. J. Wilmink *et al.*, "In vitro investigation of the biological effects associated with human dermal fibroblasts exposed to 2.52 THz radiation," *Lasers Surg. Med.*, vol. 43, no. 2, pp. 152–163, 2011, doi: 10.1002/lsm.20960.
- [10] G. J. Wilmink, B. D. Rivest, B. L. Ibey, C. L. Roth, J. Bernhard, and W. P. Roach, "Quantitative investigation of the bioeffects associated with terahertz radiation," *Opt. Interact. with Tissues Cells XXI*, vol. 7562, p. 75620L, 2010, doi: 10.1117/12.844916.
- [11] J. S. Olshevskaya, A. S. Ratushnyak, A. K. Petrov, A. S. Kozlov, and T. A. Zapara, "Effect of terahertz electromagnetic waves on neurons systems," *Proc. - 2008 IEEE Reg. 8 Int.*

- Conf. Comput. Technol. Electr. Electron. Eng. Sib. 2008*, no. February 2014, pp. 210–211, 2008, doi: 10.1109/SIBIRCON.2008.4602607.
- [12] M. R. Scarfi, M. Romanò, R. D. I. Pietro, O. Zeni, and A. Doria, “THz Exposure of Whole Blood for the Study of Biological Effects on Human Lymphocytes,” *J. Biol. Phys.*, vol. 29, no. 2, pp. 171–177, 2003.
- [13] N. Yaekashiwa, H. Yoshida, S. Otsuki, S. Hayashi, and K. Kawase, “Verification of Non-thermal Effects of 0.3–0.6 THz-Waves on Human Cultured Cells,” *Photonics*, vol. 6, no. 1, p. 33, 2019, doi: 10.3390/photonics6010033.
- [14] S. Z. Tan *et al.*, “Exposure Effects of Terahertz Waves on Primary Neurons and Neuron-like Cells Under Nonthermal Conditions,” *Biomed. Environ. Sci.*, vol. 32, no. 10, pp. 739–754, 2019, doi: 10.3967/bes2019.094.
- [15] J. Bock *et al.*, “Mammalian stem cells reprogramming in response to terahertz radiation,” *PLoS One*, vol. 5, no. 12, pp. 8–13, 2010, doi: 10.1371/journal.pone.0015806.
- [16] M. Abufadda *et al.*, “Terahertz pulses induce segment renewal via cell proliferation and differentiation overriding the endogenous regeneration program of the earthworm *Eisenia andrei*,” *Biomed. Opt. Express*, vol. 12, no. 4, pp. 1947–1961, 2021, doi: 10.1364/boe.416158.
- [17] K. T. Kim *et al.*, “High-Power Femtosecond-Terahertz Pulse Induces a Wound Response in Mouse Skin,” *Sci. Rep.*, vol. 3, pp. 1–7, 2013, doi: 10.1038/srep02296.
- [18] E. Varhalmi *et al.*, “Expression of PACAP-like compounds during the caudal regeneration of the earthworm *Eisenia fetida*,” *J. Mol. Neurosci.*, vol. 36, no. 1–3, pp. 166–174, 2008, doi: 10.1007/s12031-008-9125-z.
- [19] I. Somogyi *et al.*, “Pituitary adenylate cyclase-activating polypeptide-like compounds could modulate the activity of coelomocytes in the earthworm,” *Ann. N. Y. Acad. Sci.*, vol. 1163, pp. 521–523, 2009, doi: 10.1111/j.1749-6632.2009.04431.x.
- [20] L. Molnar *et al.*, “Immune system participates in brain regeneration and restoration of reproduction in the earthworm *Dendrobaena veneta*,” *Dev. Comp. Immunol.*, vol. 52, no. 2, pp. 269–279, 2015, doi: 10.1016/j.dci.2015.04.001.
- [21] V. Takacs, L. Molnar, B. Klimek, A. Gałuszka, A. J. Morgan, and B. Plytycz, “Exposure of

- Eisenia andrei (Oligochaeta; Lumbricidea) to cadmium polluted soil inhibits earthworm maturation and reproduction but not restoration of experimentally depleted coelomocytes or regeneration of amputated segments," *Folia Biol.*, vol. 64, no. 4, pp. 275–284, 2016, doi: 10.3409/fb64_4.275.
- [22] K. Hamana, H. Hamana, and T. Shinozawa, "Alterations in polyamine levels of nematode, earthworm, leech and planarian during regeneration, temperature and osmotic stresses," *Comp. Biochem. Physiol. -- Part B Biochem.*, vol. 111, no. 1, pp. 91–97, 1995, doi: 10.1016/0305-0491(94)00222-G.
- [23] A. Amaroli *et al.*, "The effects of photobiomodulation of 808 nm diode laser therapy at higher fluence on the in vitro osteogenic differentiation of bone marrow stromal cells," *Front. Physiol.*, vol. 9, no. FEB, pp. 1–11, 2018, doi: 10.3389/fphys.2018.00123.
- [24] T. H. Morgan, "Experimental studies of the regeneration of *Planaria maculata*," *Arch. für Entwicklungsmechanik der Org.*, vol. 7, no. 2–3, pp. 364–397, 1898, doi: 10.1007/BF02161491.
- [25] V. V. Tuchin, "Light interaction with biological tissues: overview," *Static Dyn. Light Scatt. Med. Biol.*, vol. 1884, no. July 1993, p. 234, 1993, doi: 10.1117/12.148348.
- [26] L. V. W. and H.-I. Wu, *Biomedical Optics: Principles and Imaging*. Wiley-Interscience, Hoboken, NJ, 2007.
- [27] T. Vo-Dinh (ed.), *Biomedical Photonics Handbook*. CRC Press, Boca Raton, 2014.
- [28] V. V. Tuchin, *Tissue Optics: Light Scattering Methods and Instruments for Medical Diagnosis*, 3rd ed. SPIE Press, Bellingham, WA, 2015.
- [29] J. Mobley, "Photonics and Tissue Optics," *Biomed. Photonics Handbook, Second Ed.*, pp. 21–22, 2015, doi: 10.1201/b17290-3.
- [30] V. V. Tuchin, "Light scattering study of tissues," *Physics-Uspexhi*, vol. 40, no. 5, pp. 495–515, 1997, doi: 10.1070/pu1997v040n05abeh000236.
- [31] R. Splinter and B. A. Hooper, *An Introduction to Biomedical Optics*. CRC Press, 2007.
- [32] M. Born and E. Wolf, "Principles of Optics," in *7th ed.*, 1999.
- [33] A. Akhmanov and S. Y. Nikitin, *Physical Optics*. Oxford University Press, Oxford, 1997.
- [34] M. A. Stuchly, "Interaction of radiofrequency and microwave radiation with living

- systems - A review of mechanisms," *Radiat. Environ. Biophys.*, vol. 16, no. 1, pp. 1–14, 1979, doi: 10.1007/BF01326892.
- [35] A. F. Emery, R. E. Short, A. W. Guy, K. K. Kraning, and J. C. Lin, "The numerical thermal simulation of the body when absorbing non-ionizing microwave irradiation with emphasis on the effect of different sweat models," *HEW Publ.*, vol. 78–8011, pp. 96–118, 1976.
- [36] S. Svanberg, *Atomic Molecular Spectroscopy*, 2nd ed. Berlin: Springer, 1992.
- [37] E. Pickwell and V. P. Wallace, "Biomedical applications of terahertz technology," *J. Phys. D. Appl. Phys.*, vol. 39, no. 17, 2006, doi: 10.1088/0022-3727/39/17/R01.
- [38] H. Ahlborn, X. Ji, B. Space, and P. B. Moore, "A combined instantaneous normal mode and time correlation function description of the infrared vibrational spectrum of ambient water," *J. Chem. Phys.*, vol. 111, no. 23, pp. 10622–10632, 1999, doi: 10.1063/1.480415.
- [39] B. D. Bursulaya, J. Jeon, D. A. Zichi, and H. J. Kim, "Generalized molecular mechanics including quantum electronic structure variation of polar solvents. II. A molecular dynamics simulation study of water," *J. Chem. Phys.*, vol. 108, no. 8, pp. 3286–3295, 1998, doi: 10.1063/1.475725.
- [40] A. De Santis, A. Ercoli, and D. Rocca, "On the short time motion of hydrogen-bonded molecules in supercooled water," *J. Chem. Phys.*, vol. 111, no. 10, pp. 4635–4639, 1999, doi: 10.1063/1.479741.
- [41] R. S. Keiding, "Low frequency spectroscopy of liquid water using THz-time domain spectroscopy," *J. Mol. Liq.*, vol. 101/1–3, pp. 199–218, 2002.
- [42] C. Rønne, P. O. Åstrand, and S. R. Keiding, "THz spectroscopy of liquid H₂O and D₂O," *Phys. Rev. Lett.*, vol. 82, no. 14, pp. 2888–2891, 1999, doi: 10.1103/PhysRevLett.82.2888.
- [43] E. Pickwell, B. E. Cole, A. J. Fitzgerald, V. P. Wallace, and M. Pepper, "Simulation of terahertz pulse propagation in biological systems," *Appl. Phys. Lett.*, vol. 84, no. 12, pp. 2190–2192, 2004, doi: 10.1063/1.1688448.
- [44] R. J. S. and S. P. E. H. Grant, "Dielectric Behaviour of Biological Molecules in Solution," *Oxford Clarendon*, 1978, doi: 10.1016/0307-4412(79)90015-3.

- [45] R. Pethig and D. B. Kell, "The passive electrical properties of biological systems: Their significance in physiology, biophysics and biotechnology," *Phys. Med. Biol.*, vol. 32, no. 8, pp. 933–970, 1987, doi: 10.1088/0031-9155/32/8/001.
- [46] Y. S. Lee, *Principles of Terahertz science and technology*. New York: Springer, 2009.
- [47] A. G. Markelz, A. Roitberg, and E. J. Heilweil, "Pulsed terahertz spectroscopy of DNA, bovine serum albumin and collagen between 0.1 and 2.0 THz," *Chem. Phys. Lett.*, vol. 320, no. 1–2, pp. 42–48, 2000, doi: 10.1016/s0009-2614(00)00227-x.
- [48] P. H. Bolivar, M. Brucherseifer, M. Nagel, H. Kurz, A. Bosserhoff, and R. Büttner, "Label-free probing of the binding state of DNA by time-domain terahertz sensing," *Mater. Sci. Forum*, vol. 384–385, no. June 2014, pp. 253–258, 2002.
- [49] L. V. Titova *et al.*, "Intense THz pulses cause H2AX phosphorylation and activate DNA damage response in human skin tissue," *Biomed. Opt. Express*, vol. 4, no. 4, 2013, doi: 10.1364/boe.4.000559.
- [50] B. S. Alexandrov, V. Gelev, A. R. Bishop, A. Usheva, and K. Rasmussen, "DNA breathing dynamics in the presence of a terahertz field," *Phys. Lett. Sect. A Gen. At. Solid State Phys.*, vol. 374, no. 10, pp. 1214–1217, 2010, doi: 10.1016/j.physleta.2009.12.077.
- [51] H. Hintzsche *et al.*, "Terahertz radiation at 0.380 THz and 2.520 THz does not lead to DNA damage in skin cells in vitro," *Radiat. Res.*, vol. 179, no. 1, pp. 38–45, 2013, doi: 10.1667/RR3077.1.
- [52] A. N. Bogomazova *et al.*, "No DNA damage response and negligible genome-wide transcriptional changes in human embryonic stem cells exposed to terahertz radiation," *Sci. Rep.*, vol. 5, pp. 1–6, 2015, doi: 10.1038/srep07749.
- [53] B. B. Hu and M. C. Nuss, "Imaging with terahertz waves," *Opt. Lett.*, vol. 20, no. 16, p. 1716, 1995, doi: 10.1364/ol.20.001716.
- [54] R. Williams *et al.*, "The influence of high intensity terahertz radiation on mammalian cell adhesion, proliferation and differentiation," *Phys. Med. Biol.*, vol. 58, no. 2, pp. 373–391, 2013, doi: 10.1088/0031-9155/58/2/373.
- [55] M. Borovkova *et al.*, "Investigation of terahertz radiation influence on rat glial cells," *Biomed. Opt. Express*, vol. 8, no. 1, 2017, doi: 10.1364/boe.8.000273.

- [56] M. K. D.M. Mittleman, M. Gupta, R. Neelamani, R.G. Baraniuk, J.V. Rudd, "Recent advances in terahertz imaging," *Appl. Phys. B Laser Opt*, vol. 1085–94, p. 68, 1999, doi: 10.1007/978-981-15-3235-1_10.
- [57] P. Y. Han, G. C. Cho, and X.-C. Zhang, "Time-domain transillumination of biological tissues with terahertz pulses," *Opt. Lett.*, vol. 25, no. 4, p. 242, 2000, doi: 10.1364/ol.25.000242.
- [58] M. P. DD Arnone, CM Ciesla, A Corchia, S Egusa, "Application of Terahertz (THz) technology to medical imaging," *Proc. SPIE 3823*, vol. 3828, pp. 209–19, 1999.
- [59] A. M. Ermakov, O. N. Ermakova, A. L. Popov, A. A. Manokhin, and V. K. Ivanov, "Opposite effects of low intensity light of different wavelengths on the planarian regeneration rate," *J. Photochem. Photobiol. B Biol.*, vol. 202, p. 111714, 2020, doi: 10.1016/j.jphotobiol.2019.111714.
- [60] D. P. Kuffler, "Improving the ability to eliminate wounds and pressure ulcers," *Wound Repair Regen.*, vol. 23, no. 3, pp. 312–317, 2015, doi: 10.1111/wrr.12284.
- [61] A. Schindl, H. Merwald, L. Schindl, C. Kaun, and J. Wojta, "Direct stimulatory effect of low-intensity 670 nm laser irradiation on human endothelial cell proliferation," *Br. J. Dermatol.*, vol. 148, no. 2, pp. 334–336, 2003, doi: 10.1046/j.1365-2133.2003.05070.x.
- [62] A. P. C. De Sousa *et al.*, "Effect of LED phototherapy of three distinct wavelengths on fibroblasts on wound healing: A histological study in a rodent model," *Photomed. Laser Surg.*, vol. 28, no. 4, pp. 547–552, 2010, doi: 10.1089/pho.2009.2605.
- [63] K. K. Hoe, C. S. Verma, and D. P. Lane, "Drugging the p53 pathway: Understanding the route to clinical efficacy," *Nat. Rev. Drug Discov.*, vol. 13, no. 3, pp. 217–236, 2014, doi: 10.1038/nrd4236.
- [64] F. A. H. Al-Watban, X. Y. Zhang, and B. L. Andres, "Low-level laser therapy enhances wound healing in diabetic rats: A comparison of different lasers," *Photomed. Laser Surg.*, vol. 25, no. 2, pp. 72–77, 2007, doi: 10.1089/pho.2006.1094.
- [65] S. Na, T. TruongVo, F. Jiang, J. E. Joll, Y. Guo, and A. Utreja, "Dose analysis of photobiomodulation therapy on osteoblast, osteoclast, and osteocyte," *J. Biomed. Opt.*, vol. 23, no. 07, p. 1, 2018, doi: 10.1117/1.jbo.23.7.075008.
- [66] S. Rohringer *et al.*, "The impact of wavelengths of LED light-therapy on endothelial

- cells," *Sci. Rep.*, vol. 7, no. 1, pp. 1–11, 2017, doi: 10.1038/s41598-017-11061-y.
- [67] V. Cury *et al.*, "Low level laser therapy increases angiogenesis in a model of ischemic skin flap in rats mediated by VEGF, HIF-1 α and MMP-2," *J. Photochem. Photobiol. B Biol.*, vol. 125, pp. 164–170, 2013, doi: 10.1016/j.jphotobiol.2013.06.004.
- [68] H. Kurzen, I. Wessler, C. J. Kirkpatrick, K. Kawashima, and S. A. Grando, "The non-neuronal cholinergic system of human skin," *Horm. Metab. Res.*, vol. 39, no. 2, pp. 125–135, 2007, doi: 10.1055/s-2007-961816.
- [69] A. Amaroli *et al.*, "The photobiomodulation effect of higher-fluence 808-nm laser therapy with a flat-top handpiece on the wound healing of the earthworm *Dendrobaena veneta*: a brief report," *Lasers Med. Sci.*, vol. 33, no. 1, pp. 221–225, 2018, doi: 10.1007/s10103-016-2132-3.
- [70] R. V. a N. Natuurlijke and H. Te, "Zoologische mededelingen," *Zool. Meded.*, vol. 1, no. 7, pp. 79–88, 1977.
- [71] C. A. Edwards and P. J. Bohlen, *Biology and Ecology of Earthworms*, 3rd ed. 1996.
- [72] <https://www.toppr.com/guides/biology/structural-organisation-in-animals/earthworm/>, "Earthworm." .
- [73] C. A. Edwards, *Earthworm Ecology*, 2nd ed. Nature, 2004.
- [74] <https://www.britannica.com/science/nervous-system/Annelids>, "NERVOUS SYSTEM."
- [75] A. Darmawan, R. Raffiudin, and T. Widarto, "Morphological Characters and Histology of *Pheretima darnleiensis*," *HAYATI J. Biosci.*, vol. 19, no. 1, pp. 44–48, 2012, doi: 10.4308/hjb.19.1.44.
- [76] C. Edwards and J. Lofty, "Biology of Earthworms," *Chapman Hall Ltd, London*, 1972.
- [77] K. HAMA, "The fine structure of some blood vessels of the earthworm, *Eisenia foetida*," *J. Biophys. Biochem. Cytol.*, vol. 7, no. 4, pp. 717–724, 1960, doi: 10.1083/jcb.7.4.717.
- [78] P. Engelmann, Y. Hayashi, K. Bodó, and L. Molnár, *New Aspects of Earthworm Innate Immunity: Novel Molecules and Old Proteins With Unexpected Functions*. Elsevier Inc., 2016.
- [79] P. W. Reddien and A. Sánchez Alvarado, "Fundamentals of planarian regeneration,"

- Annu. Rev. Cell Dev. Biol.*, vol. 20, pp. 725–757, 2004, doi: 10.1146/annurev.cellbio.20.010403.095114.
- [80] S. M. Da Silva, P. B. Gates, and J. P. Brockes, “The newt ortholog of CD59 is implicated in proximodistal identity during amphibian limb regeneration,” *Dev. Cell*, vol. 3, no. 4, pp. 547–555, 2002, doi: 10.1016/S1534-5807(02)00288-5.
- [81] A. A. Garza-Garcia, P. C. Driscoll, and J. P. Brockes, “Evidence for the local evolution of mechanisms underlying limb regeneration in salamanders,” *Integr. Comp. Biol.*, vol. 50, no. 4, pp. 528–535, 2010, doi: 10.1093/icb/icq022.
- [82] K. D. Poss, “Advances in understanding tissue regenerative capacity and mechanisms in animals,” *Nat. Rev. Genet.*, vol. 11, no. 10, pp. 710–722, 2010, doi: 10.1038/nrg2879.
- [83] S. J. Cho *et al.*, “Up-regulation of multiple serine proteinases during earthworm tail regeneration,” *Invertebr. Reprod. Dev.*, vol. 40, no. 2–3, pp. 103–108, 2001, doi: 10.1080/07924259.2001.9652710.
- [84] P. J. Edward, C.A. and Bohlen, “Earthworm Physiology. In: Biology and Ecology of Earthworms,” *Chapman Hall, London SEI SHN*, pp. 71-88., 1996.
- [85] L. Zhinkin, “The influence of the nervous system on regeneration in *Rhynchelmis limosella* hof,” *J. Exp. Zool.*, vol. 73, no. 1, pp. 43–65, 1936, doi: 10.1002/jez.1400730104.
- [86] C. Yoshida-Noro, M. Myohara, F. Kobari, and S. Tochinai, “Nervous system dynamics during fragmentation and regeneration in *Enchytraeus japonensis* (Oligochaeta, Annelida),” *Dev. Genes Evol.*, vol. 210, no. 6, pp. 311–319, 2000, doi: 10.1007/s004270050318.
- [87] T. L. Krause, H. M. Fishman, M. L. Ballinger, and G. D. Bittner, “Extent and mechanism of sealing in transected giant axons of squid and earthworms,” *J. Neurosci.*, vol. 14, no. 11, pp. 6638–6651, 1994, doi: 10.1523/jneurosci.14-11-06638.1994.
- [88] M. L. Ballinger, A. R. Blanchette, T. L. Krause, M. E. Smyers, H. M. Fishman, and G. D. Bittner, “Delaminating myelin membranes help seal the cut ends of severed earthworm giant axons,” *J. Neurobiol.*, vol. 33, no. 7, pp. 945–960, 1997, doi: 10.1002/(SICI)1097-4695.
- [89] A. B. Lore *et al.*, “Rapid induction of functional and morphological continuity between

- severed ends of mammalian or earthworm myelinated axons," *J. Neurosci.*, vol. 19, no. 7, pp. 2442–2454, 1999, doi: 10.1523/jneurosci.19-07-02442.1999.
- [90] S. K. Park, S. J. Cho, and S. C. Park, "Histological observations of blastema formation during earthworm tail regeneration," *Invertebr. Reprod. Dev.*, vol. 57, no. 2, pp. 165–169, 2013, doi: 10.1080/07924259.2012.713872.
- [91] A. L. Mescher, "The cellular basis of limb regeneration in urodeles," *Int. J. Dev. Biol.*, vol. 40, no. 4, pp. 785–795, 1996, doi: 10.1387/ijdb.8877452.
- [92] C. R. Kintner and J. P. Brockes, "Monoclonal antibodies identify blastemal cells derived from dedifferentiating muscle in newt limb regeneration," *Nature*, vol. 308, no. 5954, pp. 67–69, 1984, doi: 10.1038/308067a0.
- [93] C. M. Casimir, P. B. Gates, R. K. Patient, and J. P. Brockes, "Evidence for dedifferentiation and metaplasia in amphibian limb regeneration from inheritance of DNA methylation," *Development*, vol. 104, no. 4, pp. 657–668, 1988.
- [94] K. Muneoka, W. F. Fox, and S. V. Bryant, "Cellular contribution from dermis and cartilage to the regenerating limb blastema in axolotls," *Dev. Biol.*, vol. 116, no. 1, pp. 256–260, 1986, doi: 10.1016/0012-1606(86)90062-X.
- [95] M. Maden, "The role of Schwann cells in paradoxical regeneration in the axolotl," *J. Embryol. Exp. Morphol.*, vol. Vol.41, no. 1972, pp. 1–13, 1977.
- [96] J. P. Arsanto, M. Diano, Y. Thouveny, J. P. Thiery, and G. Levi, "Patterns of tenascin expression during tail regeneration of the amphibian urodele *Pleurodeles waltl*," *Development*, vol. 109, no. 1, pp. 177–188, 1990.
- [97] H. Onda, M. L. Poulin, R. A. Tassava, and I. M. Chiu, "Characterization of a newt tenascin cDNA and localization of tenascin mRNA during newt limb regeneration by in situ hybridization," *Dev. Biol.*, vol. 148, no. 1, pp. 219–232, 1991, doi: 10.1016/0012-1606(91)90331-V.
- [98] Y. Wei, E. V. Yang, K. P. Klatt, and R. A. Tassava, "Monoclonal Antibody MT2 Identifies the Urodele α 1 Chain of Type XII Collagen, a Developmentally Regulated Extracellular Matrix Protein in Regenerating Newt Limbs," *Developmental Biology*, vol. 168, no. 2, pp. 503–513, 1995, doi: 10.1006/dbio.1995.1098.
- [99] E. M. Tanaka and P. W. Reddien, "The Cellular Basis for Animal Regeneration," *Dev. Cell*,

- vol. 21, no. 1, pp. 172–185, 2011, doi: 10.1016/j.devcel.2011.06.016.
- [100] C. Streuli, “Extracellular matrix remodelling and cellular differentiation,” *Curr. Opin. Cell Biol.*, vol. 11, no. 5, pp. 634–640, 1999, doi: 10.1016/S0955-0674(99)00026-5.
- [101] C. Marcel, R. and Cardon, “Are cephalic regeneration and clitellogenesis controlled by the same neurohormone in the lumbricid, *Eisenia foetida*?,” *J. Physiol. (Paris)*, vol. 78(6), pp. 574–578, 1982.
- [102] E. V. Yang and S. V. Byant, “Developmental regulation of a matrix metalloproteinase during regeneration of axolotl appendages,” *Dev. Biol.*, vol. 166, no. 2, pp. 696–703, 1994, doi: 10.1006/dbio.1994.1348.
- [103] R. S. Weis and T. K. Gaylord, “Lithium niobate: Summary of physical properties and crystal structure,” *Appl. Phys. A Solids Surfaces*, vol. 37, no. 4, pp. 191–203, 1985, doi: 10.1007/BF00614817.
- [104] J. Hebling, G. Almási, I. Kozma, and J. Kuhl, “Velocity matching by pulse front tilting for large area THz-pulse generation,” *Opt. Express*, vol. 10, no. 21, p. 1161, 2002, doi: 10.1364/oe.10.001161.
- [105] J. Hebling, “Derivation of the pulse front tilt caused by angular dispersion,” *Opt. Quantum Electron.*, vol. 28, no. 12, pp. 1759–1763, 1996, doi: 10.1007/BF00698541.
- [106] J. Hebling, K.-L. Yeh, M. C. Hoffmann, B. Bartal, and K. A. Nelson, “Generation of high-power terahertz pulses by tilted-pulse-front excitation and their application possibilities,” *J. Opt. Soc. Am. B*, vol. 25, no. 7, p. B6, 2008, doi: 10.1364/josab.25.0000b6.
- [107] J. A. Fülöp, L. Pálfalvi, G. Almási, and J. Hebling, “Design of high-energy THz sources based on optical rectification,” *Proc. - TERA-MIR 2009, NATO Adv. Res. Work. Terahertz Mid Infrared Radiat. Basic Res. Pract. Appl.*, vol. 18, no. 12, pp. 21–22, 2009, doi: 10.1109/TERAMIR.2009.5379649.
- [108] J. A. Fülöp, L. Pálfalvi, G. Almási, and J. Hebling, “Design of high-energy THz sources based on optical rectification,” *Opt. InfoBase Conf. Pap.*, vol. 18, no. 12, pp. 4439–4444, 2009.
- [109] C. W. Berry, N. Wang, M. R. Hashemi, M. Unlu, and M. Jarrahi, “Significant performance enhancement in photoconductive terahertz optoelectronics by incorporating plasmonic

- contact electrodes," *Nat. Commun.*, vol. 4, 2013, doi: 10.1038/ncomms2638.
- [110] C. Headley *et al.*, "Improved performance of GaAs-based terahertz emitters via surface passivation and silicon nitride encapsulation," *IEEE J. Sel. Top. Quantum Electron.*, vol. 17, no. 1, pp. 17–21, 2011, doi: 10.1109/JSTQE.2010.2047006.
- [111] S. Yang, M. R. Hashemi, C. W. Berry, and M. Jarrahi, "Offered by Photoconductive Emitters With Three-dimensional Contact Plasmonic Electrodes," *IEEE Trans. Terahertz Sci. Technol.*, vol. 4, no. 5, pp. 1–7, 2014.
- [112] S. Ghorbani, M. Bashirpour, J. Poursafar, M. Kolahdouz, M. Neshat, and A. Valinejad, "Thin film tandem nanoplasmonic photoconductive antenna for high performance terahertz detection," *Superlattices Microstruct.*, vol. 120, pp. 598–604, 2018, doi: 10.1016/j.spmi.2018.06.029.
- [113] S. Lepeshov *et al.*, "Boosting Terahertz Photoconductive Antenna Performance with Optimised Plasmonic Nanostructures," *Sci. Rep.*, vol. 8, no. 1, pp. 1–7, 2018, doi: 10.1038/s41598-018-25013-7.
- [114] C. W. Berry, M. R. Hashemi, S. Preu, H. Lu, A. C. Gossard, and M. Jarrahi, "Plasmonics enhanced photomixing for generating quasi-continuous-wave frequency-tunable terahertz radiation," *Opt. Lett.*, vol. 39, no. 15, p. 4522, 2014, doi: 10.1364/ol.39.004522.
- [115] F. Akbar, M. Kolahdouz, S. Larimian, B. Radfar, and H. H. Radamson, "Graphene synthesis, characterization and its applications in nanophotonics, nanoelectronics, and nanosensing," *J. Mater. Sci. Mater. Electron.*, vol. 26, no. 7, pp. 4347–4379, 2015, doi: 10.1007/s10854-015-2725-9.
- [116] G. Valdmanis, J. and Mourou, "Subpicosecond electrooptic sampling: Principles and applications," *IEEE J. Quantum Electron.*, vol. 22(1), pp. 69–78, 1986.
- [117] Q. Wu and X.-C. Zhang, "Free-space electro-optic sampling of terahertz beams," *Appl. Phys. Lett.*, vol. 3523, p. 67, 1995.
- [118] Y. S. Lee, "Principles of Terahertz science and technology," *Springer*, pp. 250–253, 2008.
- [119] P. C. M. Planken, H.-K. Nienhuys, H. J. Bakker, and T. Wenckebach, "Measurement and calculation of the orientation dependence of terahertz pulse detection in ZnTe," *J. Opt. Soc. Am. B*, vol. 18, no. 3, p. 313, 2001, doi: 10.1364/josab.18.000313.

- [120] I. Wilke and S. Sengupta, *Nonlinear Optical Techniques for Terahertz Pulse Generation and Detection—Optical Rectification and Electrooptic Sampling*. CRC Press, 2007.
- [121] M. Siebold *et al.*, “Yb:CaF₂-a new old laser crystal,” *Appl. Phys. B Lasers Opt.*, vol. 97, no. 2, pp. 327–338, 2009, doi: 10.1007/s00340-009-3701-y.
- [122] F. Druon, F. Balembois, and P. Georges, “New materials for short-pulse amplifiers,” *IEEE Photonics J.*, vol. 3, no. 2, pp. 268–273, 2011, doi: 10.1109/JPHOT.2011.2135845.
- [123] A. Lyberis *et al.*, “Effect of Yb³⁺ concentration on optical properties of Yb:CaF₂ transparent ceramics,” *Opt. Mater. (Amst.)*, vol. 34, no. 6, pp. 965–968, 2012, doi: 10.1016/j.optmat.2011.05.036.
- [124] V. Petit, J. L. Doualan, P. Camy, V. Ménard, and R. Moncorgé, “CW and tunable laser operation of YB³⁺ doped CaF₂,” *Appl. Phys. B Lasers Opt.*, vol. 78, no. 6, pp. 681–684, 2004, doi: 10.1007/s00340-004-1514-6.
- [125] A. Lucca *et al.*, “laser e To cite this version :,” pp. 2–5, 2012.
- [126] L. Su, J. Xu, Y. Xue, C. Wang, and L. Chai, “self-Q-switched laser,” vol. 13, no. 15, pp. 348–352, 2005.
- [127] M. Siebold *et al.*, “Broad-band regenerative laser amplification in ytterbium-doped calcium fluoride (Yb:CaF₂),” *Appl. Phys. B Lasers Opt.*, vol. 89, no. 4, pp. 543–547, 2007, doi: 10.1007/s00340-007-2834-0.
- [128] V. Petit, P. Camy, J. L. Doualan, X. Portier, and R. Moncorgé, “Spectroscopy of Yb³⁺: CaF₂: From isolated centers to clusters,” *Phys. Rev. B - Condens. Matter Mater. Phys.*, vol. 78, no. 8, pp. 1–12, 2008, doi: 10.1103/PhysRevB.78.085131.
- [129] G. H. Kim *et al.*, “High-power directly diode-pumped femtosecond Yb:KGW lasers with optimized parameters,” *Solid State Lasers XXIII Technol. Devices*, vol. 8959, p. 89591B, 2014, doi: 10.1117/12.2037450.
- [130] M. M. Nazarov, A. P. Shkurinov, E. A. Kuleshov, and V. V. Tuchin, “Terahertz time-domain spectroscopy of biological tissues,” *Quantum Electron.*, vol. 38, no. 7, pp. 647–654, 2008, doi: 10.1070/qe2008v038n07abeh013851.
- [131] L. Molnár, P. Engelmann, I. Somogyi, L. L. Mácsik, and E. Pollák, “Cold-stress induced

- formation of calcium and phosphorous rich chloragocyte granules (chloragosomes) in the earthworm *Eisenia fetida*,” *Comp. Biochem. Physiol. - A Mol. Integr. Physiol.*, vol. 163, no. 2, pp. 199–209, 2012, doi: 10.1016/j.cbpa.2012.06.005.
- [132] P. D. N. Hebert, A. Cywinska, S. L. Ball, and J. R. DeWaard, “Biological identifications through DNA barcodes,” *Proc. R. Soc. B Biol. Sci.*, vol. 270, no. 1512, pp. 313–321, 2003, doi: 10.1098/rspb.2002.2218.
- [133] C. Lombosi, G. Polónyi, M. Mechler, Z. Ollmann, J. Hebling, and J. A. Fülöp, “Nonlinear distortion of intense THz beams,” *New J. Phys.*, vol. 17, no. 8, p. 83041, 2015, doi: 10.1088/1367-2630/17/8/083041.
- [134] A. S. John D. Bancroft, *Theory and practice of histological techniques*. 1990.
- [135] M. R. Hamblin, Y.-Y. Huang, and V. Heiskanen, “Non-mammalian Hosts and Photobiomodulation: Do All Life-forms Respond to Light?,” *Photochem. Photobiol.*, no. 13, 2018, doi: 10.1111/php.12951.
- [136] S. Romanenko, R. Begley, A. R. Harvey, L. Hool, and V. P. Wallace, “The interaction between electromagnetic fields at megahertz, gigahertz and terahertz frequencies with cells, tissues and organisms: Risks and potential,” *J. R. Soc. Interface*, vol. 14, no. 137, 2017, doi: 10.1098/rsif.2017.0585.
- [137] E. E. Zattara and A. E. Bely, “Evolution of a novel developmental trajectory: Fission is distinct from regeneration in the annelid *Pristina leidyi*,” *Evol. Dev.*, vol. 13, no. 1, pp. 80–95, 2011, doi: 10.1111/j.1525-142X.2010.00458.x.
- [138] M. Weidhase, C. Helm, and C. Bleidorn, “Morphological investigations of posttraumatic regeneration in *Timarete cf. punctata* (Annelida: Cirratulidae),” *Zool. Lett.*, vol. 1, no. 1, pp. 1–16, 2015, doi: 10.1186/s40851-015-0023-2.
- [139] H. Herlant-Meewis, “Regeneration in Annelids,” *Adv. Morphog.*, vol. 4, pp. 155–215, 1964.
- [140] M. Mitsushima *et al.*, “Revolving movement of a dynamic cluster of actin filaments during mitosis,” *J. Cell Biol.*, vol. 191, no. 3, pp. 453–462, 2010, doi: 10.1083/jcb.201007136.
- [141] E. E. Zattara, K. W. Turlington, and A. E. Bely, “Long-term time-lapse live imaging reveals extensive cell migration during annelid regeneration,” *BMC Dev. Biol.*, vol. 16, no. 1, pp.

- 1–21, 2016, doi: 10.1186/s12861-016-0104-2.
- [142] S. Yamazaki *et al.*, “Actin polymerization is activated by terahertz irradiation,” *Sci. Rep.*, vol. 8, no. 1, pp. 1–7, 2018, doi: 10.1038/s41598-018-28245-9.
- [143] T. Yamazaki *et al.*, “Mitochondrial DNA drives abscopal responses to radiation that are inhibited by autophagy,” *Nat. Immunol.*, vol. 21, no. 10, pp. 1160–1171., 2020, doi: 10.1038/s41590-020-0751-0.
- [144] L. Zhu and A. I. Skoultchi, “Coordinating cell proliferation and differentiation,” *Curr. Opin. Genet. Dev.*, vol. 11, no. 1, pp. 91–97, 2001, doi: 10.1016/S0959-437X(00)00162-3.
- [145] J. I. Fabrikant, “The kinetics of cellular proliferation in regenerating liver,” *J. Cell Biol.*, vol. 36, no. 3, pp. 551–565, 1968, doi: 10.1083/jcb.36.3.551.
- [146] L. V. Titova *et al.*, “Intense THz pulses down-regulate genes associated with skin cancer and psoriasis: A new therapeutic avenue,” *Sci. Rep.*, vol. 3, no. August, 2013, doi: 10.1038/srep02363.
- [147] J. W. Zhao *et al.*, “Effect of terahertz pulse on gene expression in human eye cells,” *Chinese Phys. B*, vol. 28, no. 4, 2019, doi: 10.1088/1674-1056/28/4/048703.
- [148] C. M. Hough *et al.*, “Topology-Based Prediction of Pathway Dysregulation Induced by Intense Terahertz Pulses in Human Skin Tissue Models,” *J. Infrared, Millimeter, Terahertz Waves*, vol. 39, no. 9, pp. 887–898, 2018, doi: 10.1007/s10762-018-0512-4.
- [149] T. Tachizaki, R. Sakaguchi, S. Terada, K.-I. Kamei, and H. Hirori, “Terahertz pulse-altered gene networks in human induced pluripotent stem cells,” *Opt. Lett.*, vol. 45, no. 21, p. 6078, 2020, doi: 10.1364/ol.402815.
- [150] M. Höckner, R. Dallinger, and S. R. Stürzenbaum, “Metallothionein gene activation in the earthworm (*Lumbricus rubellus*),” *Biochem. Biophys. Res. Commun.*, vol. 460, no. 3, pp. 537–542, 2015, doi: 10.1016/j.bbrc.2015.03.065.
- [151] G. B. Moment, “The relation of body level, temperature, and nutrition to regenerative growth,” *Physiol. Zool.*, vol. 26(2), pp. 108–117, 1953.
- [152] G. B. Moment, “Recovery and abscopal effects after inhibitory x-irradiation in earthworm regeneration,” *J. Exp. Zool.*, vol. 181, no. 1, pp. 33–39, 1972, doi:

- 10.1002/jez.1401810104.
- [153] P. U. Jepsen, D. G. Cooke, and M. Koch, "Terahertz spectroscopy and imaging - Modern techniques and applications," *Laser Photonics Rev.*, vol. 5, no. 1, pp. 124–166, 2011, doi: 10.1002/lpor.201000011.
- [154] M. Nagai, H. Yada, T. Arikawa, and K. Tanaka, "Terahertz time-domain attenuated total reflection spectroscopy in water and biological solution," *Int. J. Infrared Millimeter Waves*, vol. 27, no. 4, pp. 505–515, 2006, doi: 10.1007/s10762-006-9098-3.
- [155] X. G. Peralta, D. Lipscomb, G. J. Wilmink, and I. Echchgadda, "Terahertz spectroscopy of human skin tissue models with different melanin content," *Biomed. Opt. Express*, vol. 10, no. 6, p. 2942, 2019, doi: 10.1364/boe.10.002942.
- [156] T. T. L. Kristensen, W. Withayachumnankul, P. U. Jepsen, and D. Abbott, "Modeling terahertz heating effects on water," *Opt. Express*, no. 18, pp. 4727–4739, 2010.
- [157] C. Rossmanna and D. Haemmerich, "Review of temperature dependence of thermal properties, dielectric properties, and perfusion of biological tissues at hyperthermic and ablation temperatures," *Crit. Rev. Biomed. Eng.*, vol. 42, no. 6, pp. 467–492, 2014, doi: 10.1615/CritRevBiomedEng.2015012486.
- [158] K. Giering, O. Minet, I. Lamprecht, and G. Muller, "Review of thermal properties of biological tissues," *SPIE Opt. Eng. Press*, vol. 044, no. August 2018, pp. 45–65, 1995.
- [159] M. L. V. Ramires, C. A. Nieto Castro, Y. Nagasaka, A. Nagashima, M. J. Assael, and W. A. Wakeham, "Standard Reference Data for the Thermal Conductivity of Water," *J. Phys. Chem. Ref. Data*, vol. 24, no. 3, pp. 1377–1381, 1995, doi: 10.1063/1.555963.
- [160] L. Li, M. Liang, B. Yu, and S. Yang, "Analysis of thermal conductivity in living biological tissue with vascular network and convection," *Int. J. Therm. Sci.*, vol. 86, pp. 219–226, 2014, doi: 10.1016/j.ijthermalsci.2014.07.006.
- [161] T. Kujawska, W. Secomski, E. Kruglenko, K. Krawczyk, and A. Nowicki, "Determination of tissue thermal conductivity by measuring and modeling temperature rise induced in tissue by pulsed focused ultrasound," *PLoS One*, vol. 9, no. 4, 2014, doi: 10.1371/journal.pone.0094929.
- [162] C. Vicario, A. V. Ovchinnikov, S. I. Ashitkov, M. B. Agranat, V. E. Fortov, and C. P. Hauri, "Generation of 09-mJ THz pulses in DSTMS pumped by a Cr:Mg₂SiO₄ laser," *Opt. Lett.*,

vol. 39, no. 23, p. 6632, 2014, doi: 10.1364/ol.39.006632.

- [163] M. H. Abufadda *et al.*, "Absorption of Pulsed Terahertz and Optical Radiation in Earthworm Tissue and Its Heating Effect," *J. Infrared, Millimeter, Terahertz Waves*, no. 0123456789, 2021, doi: 10.1007/s10762-021-00827-1.